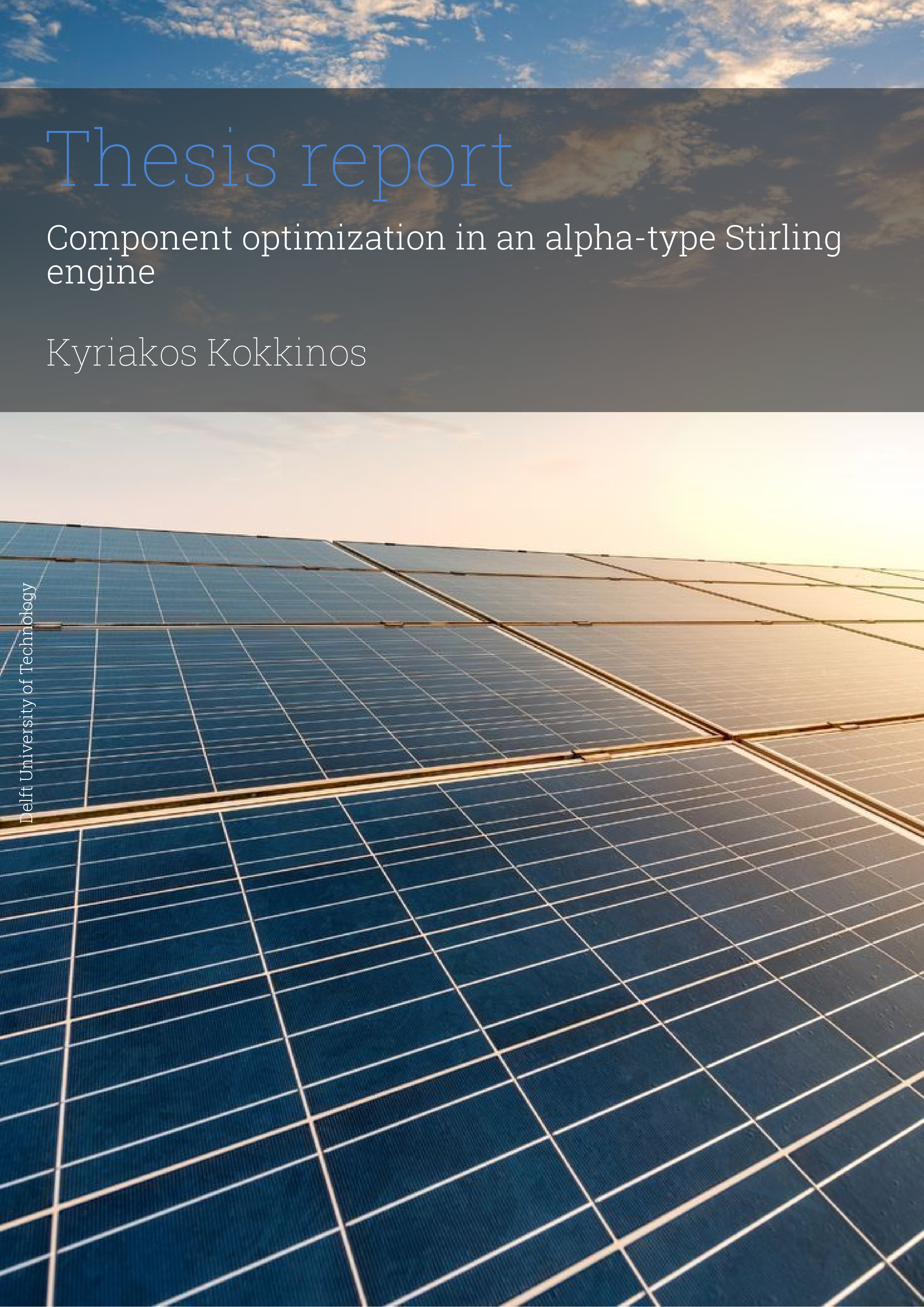

Thesis report

Component optimization in an alpha-type Stirling engine

Kyriakos Kokkinos

Delft University of Technology

Thesis report

Component optimization in an alpha-type Stirling engine

by

Kyriakos Kokkinos

Supervisor:	Prof. Dr. ir. K.Hooman
Co-Supervisor:	Dr. E. Zanetti
Company supervisor:	A. Agapiou
Faculty:	Faculty of Mechanical Engineering, Delft, Netherlands
Department:	Process and Energy department, Delft, Netherlands
Company:	EnergyIntel Services Ltd, Nicosia, Cyprus

TU Delft

Confidentiality notice

This document is a redacted version of the thesis, ”Component optimization in an alpha-type Stirling engine,” prepared for public distribution.

Certain data, including specific design parameters, proprietary model details, experimental results, and commercial specifications related to the ”Electron247” system, have been removed to protect the intellectual property and confidential information of EnergyIntel Services Ltd.

For access to the complete, unredacted version of this thesis for academic or research purposes, a formal request must be submitted to EnergyIntel Services Ltd.

Contact: EnergyIntel Services Ltd. Nicosia, Cyprus

Abstract

The increasing integration of intermittent renewable energy sources into the global energy grid necessitates the development of efficient and reliable long-duration energy storage systems. The Electron247, a thermal energy storage device developed by EnergyIntel Services, utilizes an alpha-type Stirling engine for heat-to-power conversion. However, the engine's baseline performance is a significant bottleneck, operating at a simulated [redacted] with a thermal efficiency of [redacted], which limits the overall round-trip efficiency of the system.

This thesis presents a systematic approach to improve the power output and thermal efficiency of the Electron247 system through the parametric optimization of its Stirling engine components. A specialized third-order, quasi-steady thermodynamic model was developed to accurately simulate the engine's performance, incorporating critical loss mechanisms such as imperfect heat transfer, pressure drops, regenerator ineffectiveness, and mechanical friction. The model's predictive accuracy was validated using Helium as the working fluid, showing strong correlation (average error below 7%) with experimental data from two operational units in Masdar City, Abu Dhabi.

Leveraging the validated model, a multi-objective optimization was performed using the Non-dominated Sorting Genetic Algorithm II (NSGA-II). The optimization aimed to simultaneously maximize thermal efficiency and power output by varying ten key geometric parameters of the engine's heater, cooler, and regenerator, subject to manufacturing and system-level constraints. The results produced a Pareto-optimal front of designs offering significant performance gains over the baseline configuration. Analysis of the optimal designs revealed that the regenerator's geometry (specifically, its total volume and wire mesh characteristics) was the most critical factor in determining engine performance. Notably, the ”Maximum Efficiency” design achieved a thermal efficiency of [redacted], while the balanced ”Closest to Ideal” design improved both power output to [redacted] and efficiency to [redacted]. Depending on the design choice, from a balanced-performance model to a maximum-efficiency configuration, these enhancements result in an additional 800 to 1,100 tons of CO2 emissions being spared per unit, demonstrating the critical impact of component-level optimization on the viability and environmental benefits of thermal energy storage technologies.

Acknowledgments

I would like to acknowledge that this work would not have been possible without the assistance of several individuals. The support I received throughout the entire duration of this project enabled me to perform at the maximum of my capabilities.

First of all, I would like to thank my supervising professors, Dr. Kamel Hooman and Dr. Emanuele Zanetti. Their profound expertise and knowledge enabled me to fulfill the objectives of the thesis. Their doors were always open for engaging in thoughtful discussions, creating an environment where I felt both supported and intellectually challenged.

Secondly, I would like to thank the people at EnergyIntel services and the company itself for providing me with the opportunity to conduct my thesis project with them. I would like to specifically point out that this research would not have been possible without their support, trust, and the real-world environment in which it was conducted. My gratitude goes mainly to the entire team at the R&D department, for their practical support, insightful discussions, and for making my time at EnergyIntel both productive and enjoyable.

Moving on, I would like to thank the EKO Cyprus Limited Scholarships Foundation for covering my tuition fees through the ’Proud of Youth’ scholarship program.

Lastly, but most importantly, I would like to express my deepest gratitude to my parents. Their invaluable and unwavering support has been the cornerstone of my academic pursuits, including this thesis. This project marks the culmination of a journey that, without them, would not have even begun. Through their selfless sacrifices, they paved the way for me to explore and excel in a field of my passion. Their love and encouragement were the primary catalysts for my perseverance and success. Every achievement, past, present, and future, I dedicate to them.

Contents

Nomenclature

Abbreviations

Abbreviation	Definition
AC	Alternating Current
AISI	Aluminium-Silicon (Alloy)
CFD	Computational Fluid Dynamics
CHP	Combined Heat and Power
CO_2	Carbon Dioxide
CSP	Concentrated Solar Power
DP	Displacer Piston
GA	Genetic Algorithms
GHG	Greenhouse Gas
HEX	Heat Exchanger
HTF	Heat Transfer Fluid
IEA	International Energy Agency
IRENA	International Renewable Energy Agency
ISA	International Standard Atmosphere
LBE	Lead-Bismuth Eutectic
LCOS	Levelized Cost Of Storage
LINMAP	Linear Programming Technique for Multidimensional Analysis of Preference
LMTD	Log Mean Temperature Difference
mCHP	micro-Combined Heat and Power
MOO	Multi-Objective Optimization
NIMA	Nature-Inspired Metaheuristic Algorithms
NSGA-II	Non-dominated Sorting Genetic Algorithm II
NTU	Number of Transfer Units
ODE	Ordinary Differential Equation
PCM	Phase Change Material
PCP	Parallel Coordinates Plot
PP	Power Piston
PSVL	Polytropic analysis of Stirling engine with Various Losses
PV	Photovoltaic
RPM	Revolutions Per Minute
TES	Thermal Energy Storage
VAC	Volts Alternating Current

Symbols

Symbol	Definition	Unit
A	Area	[m^2]
a	Relative transverse pitch (tube banks)	[-]
A_R, A_ω	Relative amplitude of fluid displacement	[-]
b	Relative longitudinal pitch (tube banks)	[-]
C	Heat capacity ratio (C_{min}/C_{max})	[-]
C_c	Cold fluid heat capacity rate	[W/K]
C_f	Friction factor (regenerator)	[-]
C_h	Hot fluid heat capacity rate	[W/K]
c_p	Specific heat capacity at constant pressure	[J/(kg K)]
c_v	Specific heat capacity at constant volume	[J/(kg K)]
D	Diameter	[m]
D_h	Hydraulic diameter	[m]
f	Darcy friction factor	[-]
h	Heat transfer coefficient	[W/(m^{2}K)]
k	Thermal conductivity	[W/(m K)]
L	Length	[m]
m	Mass	[kg]
$\dot{m}$	Mass flow rate	[kg/s]
NTU	Number of Transfer Units	[-]
Nu	Nusselt number (hD_h/k)	[-]
P	Pressure	[Pa]
Pe	Péclet number ($Re \cdot Pr$)	[-]
Pr	Prandtl number ($c_p\mu/k$)	[-]
Q	Heat transfer	[J]
$\dot{Q}$	Heat transfer rate	[W]
R	Specific gas constant	[J/(kg K)]
Re	Reynolds number ($\rho v D_h/\mu$)	[-]
Re_m, Re_ω	Dimensionless frequency of oscillation	[-]
Re_{max}	Maximum Reynolds number (range definition)	[-]
Re_w	Dimensionless frequency (range definition)	[-]
R_{conv}	Convective thermal resistance	[K/W]
R_{tot}	Total thermal resistance	[K/W]
R_w	Thermal resistance of wall	[K/W]
T	Temperature	[K] or [$^\circ$C]
t	Time	[s]
t	Pitch-to-diameter ratio (tube bundles)	[-]
U	Overall heat transfer coefficient	[W/(m^{2}K)]
U	Velocity (alternative to v)	[m/s]
V	Volume	[m^3]
v	Velocity	[m/s]
W	Work	[J]
$\dot{W}$	Power	[W]
θ	Crank angle	[deg]
α_1, α_2	Constants in friction factor correlation form	[-]
γ	Ratio of specific heats (c_p/c_v)	[-]

Symbol	Definition	Unit
Δ	Difference or change	(units vary)
ϵ	Volumetric porosity	[-]
η	Efficiency	[-]
λ	Thermal conductivity (alternative to k)	[W/(m K)]
μ	Dynamic viscosity	[Pa s]
ν	Kinematic viscosity (μ/ρ)	[m^2/s]
ρ	Density	[kg/m^3]
σ	Stefan-Boltzmann constant	[W/(m^{2}K^4)]
ϕ	Total wire surface area factor (regenerator)	[-]
ϕ_{net}	Specific net heat transfer area (regenerator)	[-]
ω	Angular velocity / frequency	[rad/s]

1

Introduction

The global energy sector is undergoing a critical transformation, driven by the need to mitigate climate change as mandated by international accords, such as the Paris Agreement [1]. Humanity's approach to energy production, distribution, and consumption is undergoing a profound socio-technical transformation. The established goal set by international agreements is to limit carbon dioxide emissions resulting from human behaviour, thereby limiting global warming to well below 2 °C, preferably 1.5 °C, compared to pre-industrial levels.

This transformation directly influences the energy production sector. According to the International Renewable Energy Agency (IRENA), limiting global warming to 1.5 °C requires reducing carbon dioxide emissions by 37 gigatonnes from 2022 levels. Furthermore, the energy sector must achieve net-zero emissions by 2050 [2].

To achieve these goals, a fundamental shift away from the oil and gas producing methods is necessary. This shift is necessitated by the implementation of renewable energy sources in future energy grids. This can be observed from Figure 1.1a, which presents two potential scenarios evaluating the share of energy production in ten and twenty-five years. Sky 2050 represents a case where emissions and global warming limitation are prioritized, while Archipelagos represents the scenario where energy security is the primary objective. In both cases, the significant increase in the renewable share, combined with a reduction in oil and gas production, is evident.

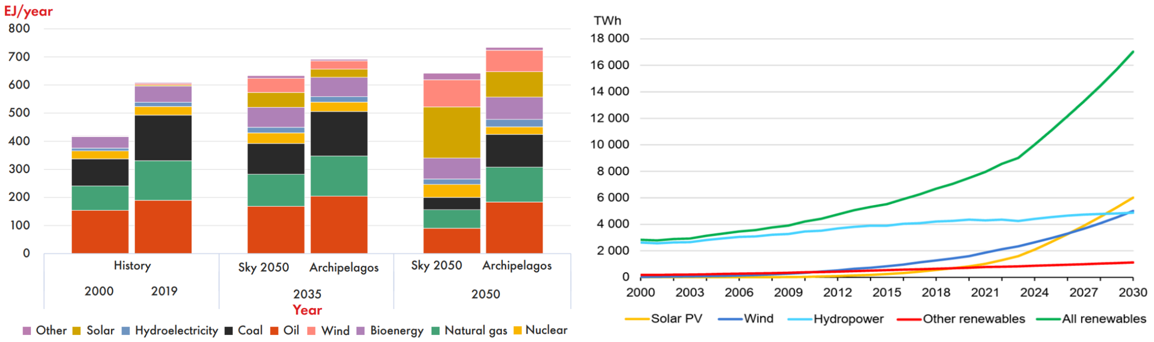

(a) The two energy sector development projections as projected by two models, Archipelagos and Sky 2050, developed from Shell [3].

(b) The projected share of renewables in the energy production sector, as predicted from the International Energy Agency (IEA) in 2024 [4].

Furthermore, the International Energy Agency (IEA) expects total renewable energy generation to reach approximately 17,000 TWh by 2030 (Figure 1.1b), highlighting the growth of the renewable energy sector. Among the distinct green power sources, solar energy is considered the most promising, with expectations to surpass both wind and hydropower for the first time towards the end of the decade. This is primarily due to the increasing efficiency and decreasing production costs of photovoltaic panels.

The increasing installation of renewable energy infrastructure has given rise to the concept of 'energy security', a term of growing importance in policy and academic discourse. Due to the inherent intermittency of renewables, particularly solar power, the widespread and reliable integration of solar power into energy grids is hindered. This is visualized in Figure 1.2a, specifically during the middle of the day, when solar power generation is at its maximum, resulting in a significant drop in net grid electricity demand. This phenomenon is growing in tandem with the increasing number of solar installations over the years.

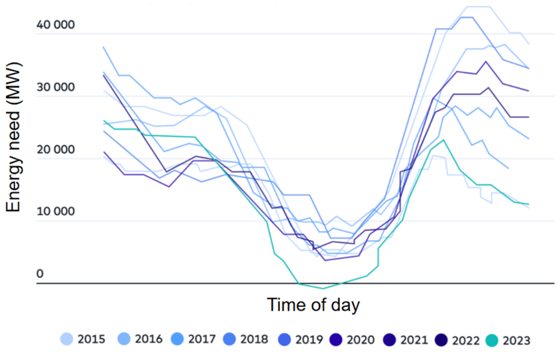

(a) The energy demand of the German grid over a day, and the transition over the years [5].

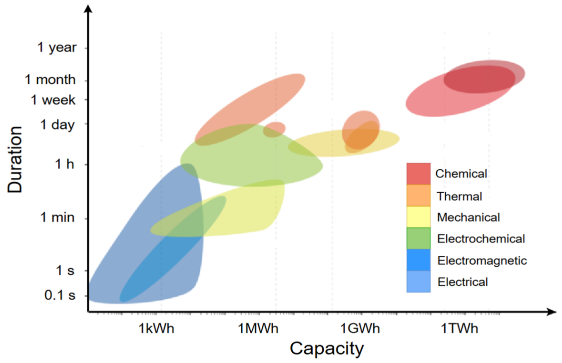

(b) The discharge duration and capacity capabilities of different energy storage systems [6].

The most promising solution for overcoming this limitation requires implementing storage infrastructure to ensure a stable and reliable renewable energy supply. As cited from the International Renewable Energy Agency, 'Storage will be critical to achieving energy system flexibility, which has brought attention to innovative storage solutions. Ultimately, the goal is partial decoupling of electricity generation and consumption, enabling the increased installation of renewable energy sources' [7]. Several different mechanisms exist for energy storage, each with its own potential capacity, charge and discharge time scales, and cost. A concise overview is presented in Figure 1.2b.

1.1. Thermal energy storage

Thermal energy storage (TES) has been identified as a crucial enabling technology [8–10] for storing renewable energy. TES technology is particularly well-suited for long-duration energy storage due to its fundamental heat transfer timescale characteristics [11]. It can be categorized into two distinct subdivisions, latent and sensible heat storage. This categorization depends on whether the storage medium undergoes a phase change during the charge and discharge phases (latent heat) or not (sensible heat).

1.2. Electron247 - Problem statement

Electron247 is a long-duration thermal energy storage device, developed by EnergyIntel Services, a Cyprus-based renewable energy company, capable of storing a maximum of 550kWh_{th}. The device utilizes an Aluminium-Silicon (Al-Si) alloy as a Phase Change Material (PCM), leveraging its high latent heat of fusion. This material is advantageous over commonly used molten salts due to its lower melting point and high energy density.

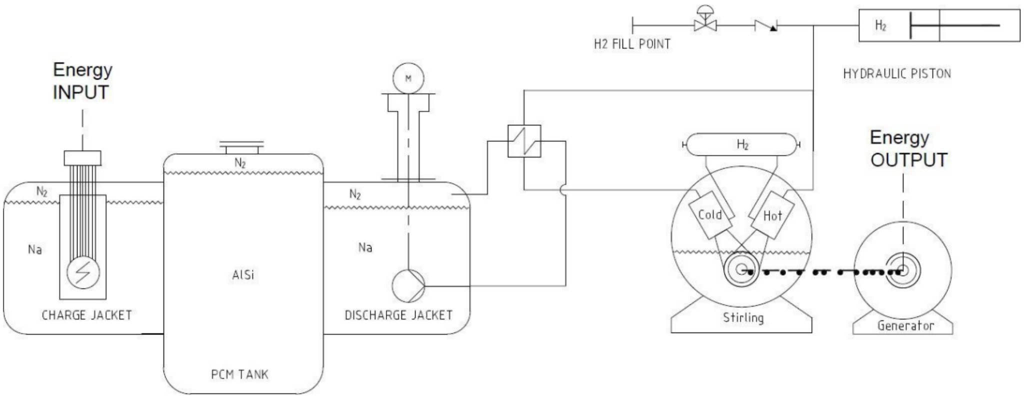

Figure 1.3: Schematic overview of the Electron247 thermal energy storage system, illustrating the main functional units: charging circuit with heat input, thermal storage tank (PCM/AlSi), and discharging circuit featuring the alpha-type Stirling engine coupled to an electrical generator for energy output. (Source: Adapted from EnergyIntel Services documentation).

Figure 1.3 depicts the main components of the storage device. The system's primary energy source is a photovoltaic array. Electrical energy is converted into thermal energy via electrical resistive heaters. These heaters heat a jacket containing liquid sodium, which in turn melts the Phase Change Material (PCM) within a storage tank, thereby charging the system. During the discharge cycle, the liquid sodium flows through a discharge jacket, transferring heat to an alpha-type Stirling engine. The Stirling engine, operating exclusively during discharge, converts this thermal energy into mechanical energy. The engine's crankshaft is directly coupled to a generator, which performs the final conversion of mechanical energy back into electrical energy. The engine coupled to the generator is capable of operating at a constant power output of 13 kW_e for several hours. The detailed technical specifications of Electron247 can be found in Appendix A

The phase change material (PCM) is selected for its high latent heat of fusion. This can be observed in Figure 1.4, with the Aluminum-Silicon alloy (circled in red) being ranked among the materials with the highest density-specific latent heats. The latent heat of fusion of this material is measured at an increased 560 kJ/kg compared to 388 kJ/kg of pure Aluminum.

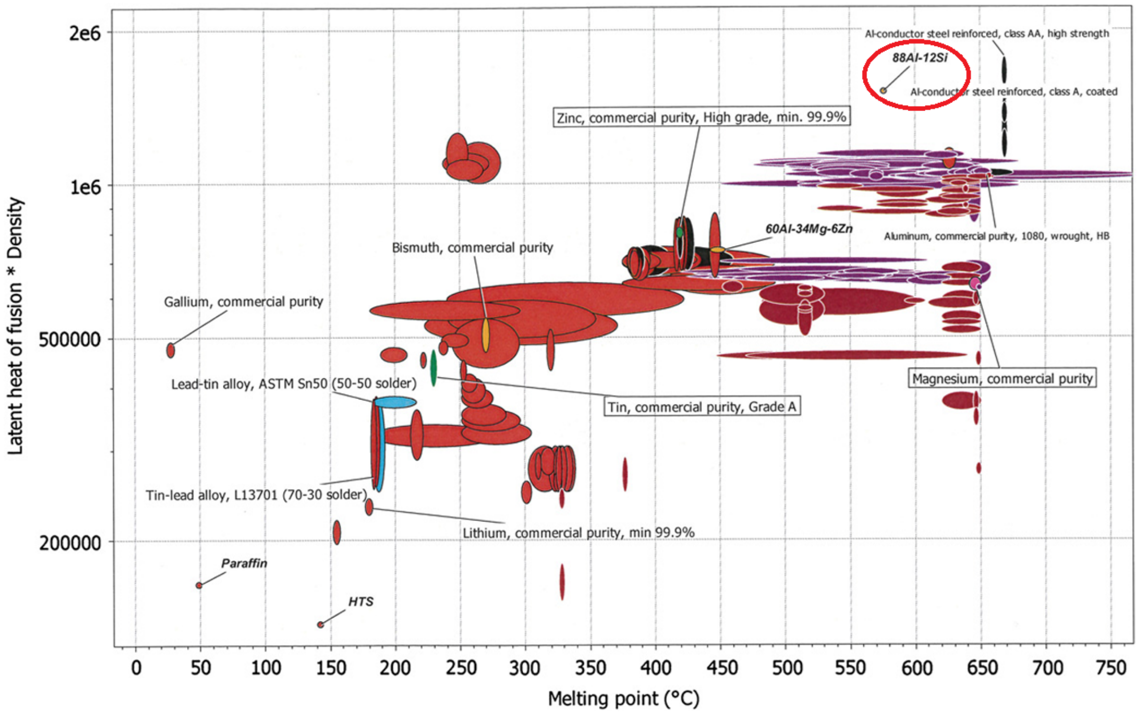

Figure 1.4: Density normalized latent heats of fusion for several metal alloys [12]

Sodium is also selected based on its enhanced thermal performance, particularly at higher temperatures. The selection of heat transfer fluids for high-temperature applications is limited. While superheated steam and helium are potential options, they exhibit inferior thermal properties compared to liquid sodium. Figure 1.5 indicates that for increased temperatures, sodium features the highest thermal conductivity compared to both gases (steam, helium), but more importantly to other liquid metals as well, namely tin (Sn) and lead-bismuth eutectic alloys (LBE).

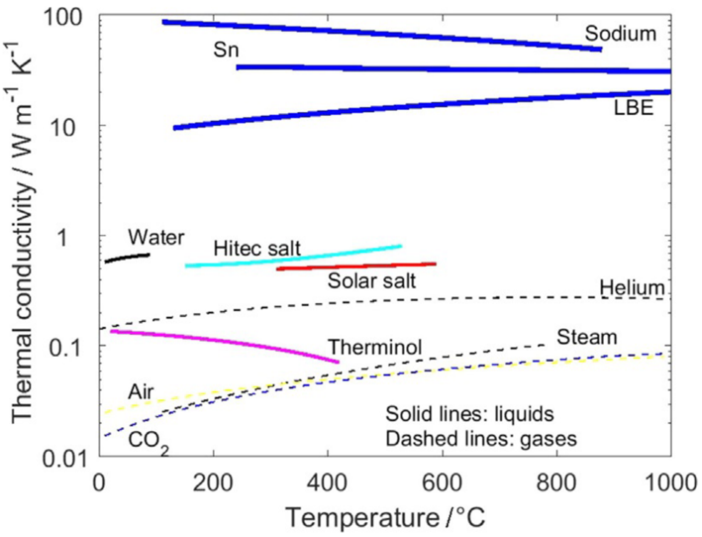

Figure 1.5: Heat conductivity for different heat transfer fluids [13]

The multiple energy conversion steps significantly reduce the overall round-trip efficiency of the device. A critical bottleneck in the system's round-trip efficiency (electricity-heat-electricity) is the heat-to-power conversion stage. The alpha-type Stirling engine, although advantageous for its external heat addition capability, currently operates at a thermal efficiency of less than 30%. This presents the most significant opportunity for system-level performance enhancement through targeted component optimization.

1.3. Research question

This thesis focuses on the development of a mathematical model of the specific Stirling machine used in EnergyIntel's Electron247. This model was used for the parametric optimization of the machine's fundamental components. The optimization procedure, which explores extensive design solutions, is bounded by a set of geometrical, functional, and resource availability constraints. The scope is summarized with the following research question:

'How can the overall efficiency and power output of a thermal energy storage device be improved, by parametric optimization of the main components of an alpha-type Stirling engine, utilized for energy transformation?'

The core research challenge stems from the fundamental laws of thermodynamics and the principle of energy conservation. The challenge lies in balancing conflicting geometric and operational parameters to optimize the engine's power output and thermal efficiency. The complexity of the problem is further amplified by the unique combination of components and materials that form Electron247. The design involves:

- An alpha-type Stirling engine coupled to a generator
- Hydrogen or helium as the working fluid, chosen for their excellent thermodynamic properties, but known for their small molecular size, which exacerbates leakage issues through seals and containment materials.
- A liquid sodium heat transfer circuit on the hot side, whose extremely low Prandtl number requires specialized heat transfer correlations distinct from those for conventional fluids.
- A stacked wire screen regenerator, whose performance is dictated by a delicate balance between heat storage capacity and flow-induced pressure drop, a relationship governed by complex empirical correlations.

This work introduces a novel perspective by focusing on the development of a systematic optimization methodology. A computational framework was developed that can efficiently determine the optimal geometric and dimensional parameters for the key components of an alpha-type Stirling engine, given specific operational constraints. As a result, the framework aims to enhance the engine's performance, approaching the practical limits of the Electron247 system.

1.4. Methodology

This section details the systematic, four-phase methodology employed to enhance the performance of the Electron247 alpha-type Stirling engine. The approach begins with the development of a specialized thermodynamic model, which is then used in an integrated optimization of the engine's key heat exchange components. The process concludes by establishing clear and actionable design rules, providing a direct pathway to a more efficient and competitive thermal energy storage system.

Phase 1: Thermodynamic model development

The foundation of this research was the development of a specialized thermodynamic model, engineered to accurately simulate the Electron247's alpha-type Stirling engine. A third-order quasi-steady model was selected, offering an effective balance between predictive efficiency and computational efficiency, which is required for extensive optimization studies. The model was adapted for the specific application by combining several models from the literature, introducing new loss mechanisms, and updating dated empirical approximations with more recent findings from the literature. To ensure the reflection of physical reality, several key loss mechanisms were incorporated, including imperfect heat transfer in the heat exchangers, conduction losses within the engine, pressure drop resulting from the fluid friction of the working gas, and mechanical friction between the engine's friction components.

Phase 2: Model validation

With the theoretical model developed, the next critical phase was to validate its predictive accuracy against experimental performance data. This process ensures that the model is a credible tool for design optimization. The validation was performed using experimental data from two operational units installed in Masdar City, Abu Dhabi. The data underwent a rigorous pre-processing phase to ensure quality and relevance. The model's predictions for power output and thermal efficiency were then compared against this processed experimental data at specified operating conditions. The model's accuracy was quantified using standard statistical metrics. The results confirmed the model's reliability, deeming it suitable for use in the subsequent optimization phase.

Phase 3: Multi-objective component optimization

Leveraging the validated model, a multi-objective optimization was executed to systematically identify component geometries that enhance the engine's performance. The Non-dominated Sorting Genetic Algorithm II (NSGA-II), a widely used and efficient metaheuristic algorithm, was employed for this task through the pymoo Python library. The optimization was driven by two simultaneous, conflicting objectives: the maximization of thermal efficiency (η) and the maximization of power output (P_{out}). The algorithm varied ten key geometric parameters of the Stirling engine, within a predefined search space, always satisfying the constrained nature of the problem. Recognizing that continuous values for dimensions are not manufacturable, the optimization was refined to a discrete process. In this final step, all geometric parameters were constrained to discrete, realistic step sizes that align with standard manufacturing capabilities and tolerances.

Phase 4: Analysis and derivation of design rules

The final phase focused on interpreting the optimization results to provide clear, actionable recommendations for EnergyIntel Services. The optimization process produced a Pareto-optimal front, a collection of non-dominated designs that represent the best possible trade-offs between maximizing efficiency and maximizing power output. A structured decision-making procedure was employed, which transforms the complex output of the optimization into a clear set of design rules and a final recommended configuration, providing a direct pathway for enhancing the Electron247 system.

2

Theoretical foundation and literature review

2.1. The Stirling engine

The invention of the engine is attributed to the Scottish clergyman Robert Stirling, who patented his first design in 1816. Despite early applications, the development and widespread adoption of Stirling engines significantly slowed during the early 20th century, largely eclipsed by advancements in internal combustion engines and the proliferation of electric motors [14].

The Stirling engine is a class of external heat engines operating on a closed regenerative thermodynamic cycle, where heat is exchanged with external thermal reservoirs. This operational principle distinguishes it from internal combustion engines and theoretically allows Stirling engines to achieve high thermal efficiencies, potentially approaching the Carnot limit for given temperature differentials [15].

$$\eta_{carnot} = 1 - \frac{T_c}{T_h} \tag{2.1}$$

This Carnot limit serves as the theoretical benchmark for Stirling engines because, in its ideal form, the cycle involves external heat transfer occurring only during the isothermal expansion (T_h) and compression (T_c) stages. The heat required for the isochoric heating phase is ideally supplied entirely by the heat stored in the regenerator during the isochoric cooling phase, making the regenerative processes internally reversible and allowing the overall cycle efficiency to match that of a Carnot engine operating between the same temperature limits.

2.1.1. Key advantages of Stirling engines

A primary advantage of the Stirling engine is its compatibility with any external heat source. Unlike an internal combustion engine, which relies on fuel combustion inside the cylinder to expand and generate work, the Stirling engine relies on an external heat reservoir from which heat is supplied. Specifically for this application, the Aluminium-Silicon alloy provides heat at a nearly constant temperature, close to the Eutectic point of the material (577°C). Operating between this high temperature and an ambient-temperature heat sink results in a large temperature differential, which provides a higher theoretical performance ceiling compared to cycles limited to lower operating temperatures.

Another critical advantage of Stirling machines is the ability to achieve high power density. Primarily, when the engine operates with helium or hydrogen as the working gas, this, in combination with the low noise and vibration of Stirling machines, presents a significant advantage for commercial applications where noise pollution is a concern.

Key advantages associated with this design include multi-fuel capability (compatibility with a wide variety of heat sources, including solar, geothermal, biomass, and waste heat), characteristically low noise emissions, and reduced vibration levels compared to piston-based internal combustion engines [14, 15].
In recent decades, there has been renewed interest in Stirling engines for various contemporary energy applications. These include solar thermal electricity generation (particularly using parabolic dish collectors), waste heat recovery systems, micro-Combined Heat and Power (mCHP) units, and potential integration with Thermal Energy Storage (TES) systems to enhance grid flexibility or provide dispatchable renewable power.

2.1.2. Engine configuration

Stirling engines are typically classified into three primary configurations: alpha, beta, and gamma. These classifications are distinguished principally by the mechanical arrangement employed to cycle the working fluid between the hot (expansion) and cold (compression) regions of the engine [15, 16].

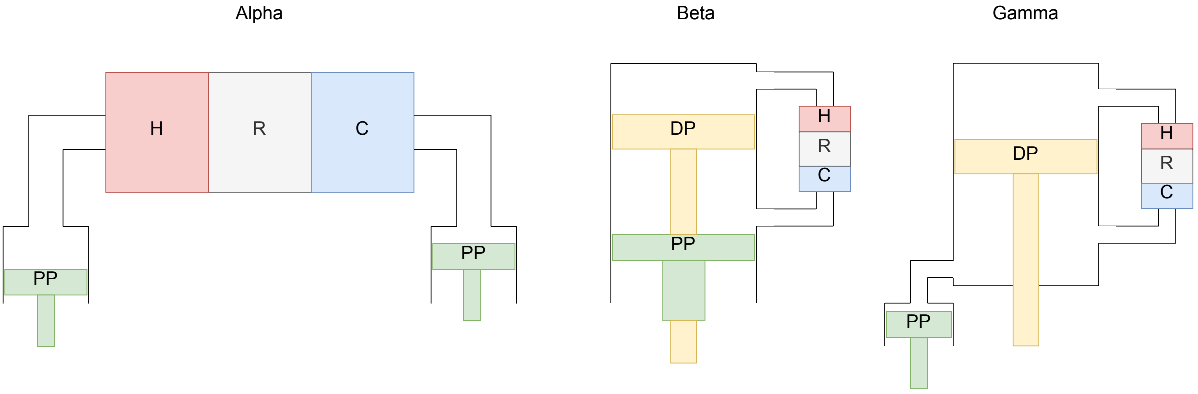

Figure 2.1: Schematic representations of the three primary Stirling engine configurations (Alpha, Beta, Gamma), illustrating the arrangement of power pistons (PP), displacer pistons (DP), heater (H), regenerator (R), and cooler (C).

The beta configuration utilizes a single cylinder that contains both a power piston and a displacer piston, operating on the same axis. The displacer piston's function is to shuttle the working gas between the hot end and the cold end of the cylinder through the heat exchangers, which are typically arranged around the cylinder or in connecting passages. The power piston extracts work from the pressure changes within the cylinder. Similar to the Beta type, the Gamma configuration uses a power piston and a displacer piston. However, they are located in separate, but connected, cylinders. The displacer shuttles the gas between the hot and cold spaces (which include the heater, regenerator, and cooler), and the power piston, located in its own cylinder connected to the cold space, extracts work. This arrangement allows for more mechanical design flexibility than the Beta type but often results in a larger ”dead volume” which can negatively impact performance [16, 17].

The alpha configuration, utilized in Electron247, is characterized by two distinct cylinders, each housing a dedicated piston. One cylinder serves as the expansion space (hot side), while the other acts as the compression space (cold side). The working fluid is transferred between these two cylinders via connecting passages, often incorporating regenerators and heat exchangers. The pistons are mechanically linked, commonly to a shared crankshaft, and operate with a defined phase difference, typically around 90 degrees, necessary to execute the thermodynamic cycle [15].

A significant technical consideration for the alpha-type engine is the requirement for robust dynamic sealing on both pistons, particularly at the hot end. Achieving effective sealing can be challenging, especially in high-pressure systems or when utilizing low-molecular-weight working fluids such as hydrogen or helium, which can impact long-term reliability and performance. Conversely, compared to the beta and gamma configurations, which often involve more complex displacer mechanisms or linkages, the fundamental mechanical design and manufacturing of the alpha-type engine can be relatively straightforward [14].

2.1.3. Engine cycle

The Stirling engine operates based on a closed thermodynamic cycle, using a gaseous working fluid. To understand its fundamental potential, we first examine the ideal Stirling cycle, which is based on the following key simplifying assumptions [17, 18]:

1. The working fluid behaves as an ideal gas.
2. Expansion and compression processes are perfectly isothermal.
3. Regeneration process is perfect (100% effectiveness, zero temperature difference between fluid and matrix at any point, and no pressure drop).
4. Isochoric processes occur instantaneously as the fluid passes through the regenerator.
5. There are no flow losses (friction) or mechanical friction.
6. Heat transfer occurs infinitely fast to maintain isothermal conditions.
7. Perfect sealing (no leakage).

The ideal cycle consists of four fundamental cyclic processes: isothermal compression, isochoric heat addition, isothermal expansion, and isochoric heat removal. During the first process (isothermal compression), heat is rejected from the gas to the external cooling stream, leading to a decrease in volume. Subsequently, the gas flows through the regenerator, at constant volume, absorbing stored heat and increasing its temperature as it moves to the heated expansion space. During the third process (isothermal expansion), work is produced as the heated working fluid expands. Finally, in the isochoric heat removal phase, the working fluid passes through the regenerator, at constant volume, cooling down and transferring heat to the regenerator matrix. The cyclic process can be observed in Figure 2.2.

The Stirling cycle is an adaptation of the Carnot cycle, where isochoric regeneration processes replace the isentropic processes of the Carnot cycle. Yet, it retains the same maximum theoretical efficiency as the Carnot cycle (Equation 2.1). The heat transferred internally during the two isochoric processes (2-3 and 4-1) is perfectly managed by the ideal regenerator; the heat rejected to the regenerator during process 4-1 is exactly recovered during process 2-3. Therefore, in the ideal case, there is no net heat exchange with the surroundings during these steps. These conditions precisely mirror the requirements for achieving the maximum possible thermodynamic efficiency defined by the Carnot limit. While real engines cannot achieve these ideal conditions, the ideal Stirling cycle provides the fundamental basis for understanding the engine's potential. These processes can be visually represented on Pressure-Volume

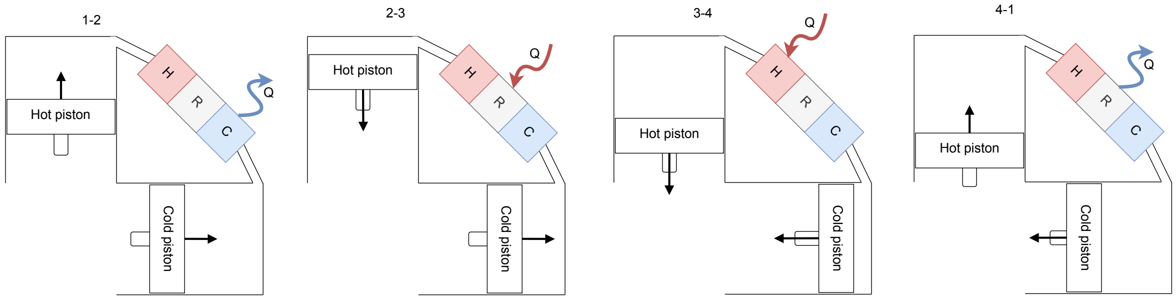

Figure 2.2: Illustration of the four processes in the ideal Stirling cycle for an alpha-type engine: 1-2 Isothermal compression (heat rejection), 2-3 Isochoric heat addition (via regenerator), 3-4 Isothermal expansion (heat addition), and 4-1 Isochoric heat rejection (via regenerator).

(P-V) and Temperature-Entropy (T-S) diagrams, illustrating the thermodynamic changes of the working fluid.

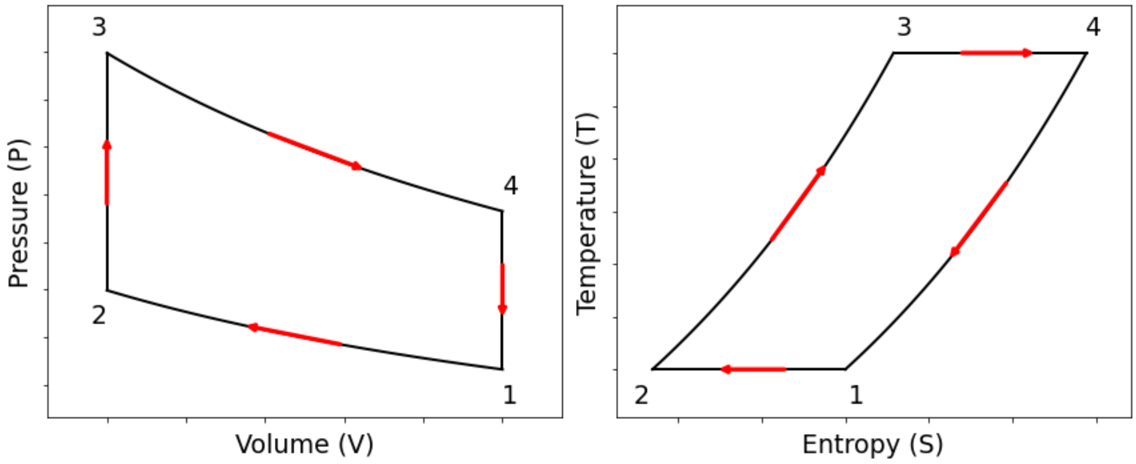

Figure 2.3: Thermodynamic diagrams for the ideal Stirling cycle: (Left) Pressure-Volume (P-V) diagram showing work done during the cycle; (Right) Temperature-Entropy (T-S) diagram illustrating heat transfer during isothermal processes and constant volume regeneration paths. The numbers correspond to the states shown in Figure 2.2

.

The ideal Stirling cycle, with its assumptions of perfect isothermal processes, flawless regeneration, and zero flow losses, provides a valuable theoretical upper limit on performance. It significantly diverges from the operation of actual Stirling engines. In reality, numerous factors prevent the attainment of this ideal cycle. These cumulative effects lead to a 'real' thermodynamic cycle that produces significantly less work and operates at lower efficiency than predicted by the ideal model.

2.1.4. Working fluids

The selection of a working fluid is a critical design parameter for Stirling engines. While various gases can be utilized, the most common choices include hydrogen, helium, and air, each presenting distinct advantages and disadvantages.

Hydrogen

Hydrogen is often preferred for applications demanding high specific power output and efficiency. Its favorable thermodynamic properties, particularly its high thermal conductivity and low viscosity, facilitate rapid heat transfer and minimize flow losses within the engine's heat exchangers and regenerator [17]. However, hydrogen's small molecular size poses significant containment challenges, leading to increased leakage rates through dynamic seals and diffusion through containment materials, especially under high-pressure and temperature conditions. Furthermore, the inherent flammability of hydrogen necessitates rigorous safety measures and specialized handling procedures, which limit its application in certain commercial or non-specialized environments.

Helium

Helium offers thermodynamic performance characteristics comparable to those of hydrogen, yielding a similar potential for high power density and efficiency. As an inert gas, it eliminates the flammability concerns associated with hydrogen. Its larger molecular size also results in lower leakage and diffusion rates compared to hydrogen, simplifying sealing requirements. The primary disadvantages of helium are its relatively high cost and limited global availability, which can impact both initial and operational expenditures. [17]

While the Stirling machine in Electron247 was initially designed and manufactured for hydrogen, due to safety concerns, it operated with helium during preliminary testing. Consequently, the complete set of data obtained from experimental measurements reveals a reduced power output and efficiency.

2.2. Detailed Electron247 configuration

The alpha-type Stirling engine of Electron247 utilizes a specific array of components to exchange heat between the heating and cooling streams of the engine, with the working gas. Two tubular, cross-flow heat exchangers are utilized, along with a stacked wire mesh regenerator. The working gas (Hydrogen or Helium) passes through the heat exchanger array, interchanging heat with the two external flows.

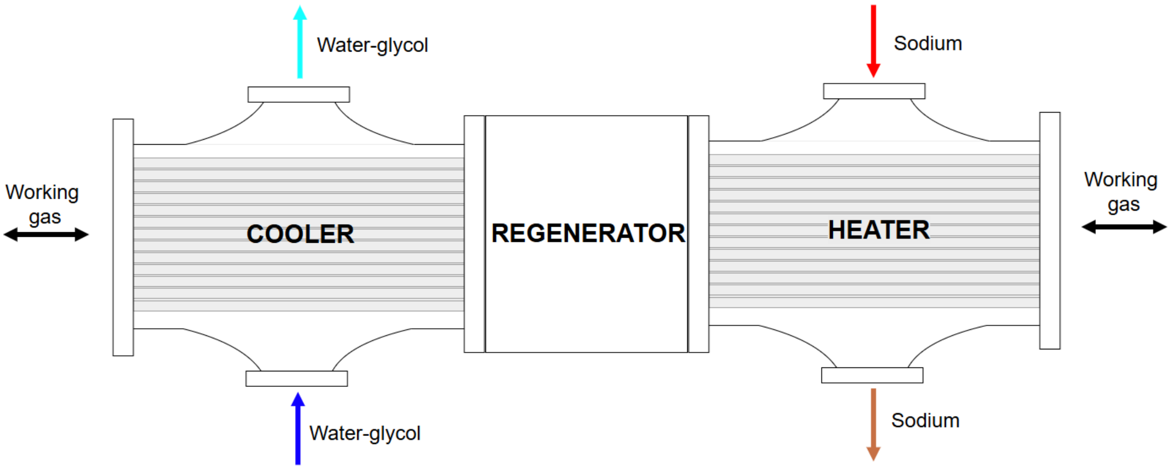

Figure 2.4: Schematic of the heat exchanger and regenerator assembly in the Electron247 Stirling engine. It illustrates the flow paths, with the working gas passing sequentially through the cooler, regenerator, and heater, while exchanging heat with the external water-glycol and sodium circuits.

2.2.1. Sodium flow

Heat is supplied to the engine via a liquid sodium heat transfer circuit. Sodium (Na) is an alkali metal with excellent thermal properties. The high boiling point, low viscosity and density, and relatively high thermal conductivity make it an ideal solution for use as an HTF in compact, high thermal capacity heat exchangers [19,20]. These characteristics make sodium advantageous when compared to conventional HTFs such as water and oil. These make sodium particularly attractive for high-temperature applications such as concentrated solar power (CSP) plants and advanced nuclear reactors. While the use of sodium as an HTF has been explored for decades, ongoing research and development continue to refine its application and address the associated challenges [21]. The heat transfer characteristics of a sodium flow differ significantly from those of water and oils. This difference in heat transfer characteristics stems from the low Prandtl number of liquid metals. The physical significance of the Prandtl number is the ratio between the kinematic viscosity and thermal diffusivity of a fluid. This means that thermal energy diffuses through sodium much faster than momentum, leading to heat transfer characteristics that are dominated by conduction within the fluid, unlike conventional fluids, where convection is paramount. Due to the increased thermal conductivity and decreased viscosity of sodium, the range of Prandtl number in sodium flows falls within the range of 0.001-0.01 compared to 1-10 for traditional HTFs [22,23].

Disadvantages and challenges of Sodium as HTF

A significant disadvantage of Sodium is the high reactivity that it presents when in contact with air or water. The reaction of sodium with water is highly exothermic and violent, producing hydrogen, which is both flammable and explosive. Sodium also reacts readily with oxygen in the air, forming sodium oxides and potentially igniting spontaneously at temperatures as low as 115°C, depending on conditions such as humidity and dispersion [24].

Another essential aspect when considering sodium as an HTF is corrosion effects occur when sodium is in contact with foreign materials, including stainless steel and carbon. These corrosion characteristics tend to influence the components with which sodium is in contact, ultimately resulting in reduced life expectancy of the components [25].

Water-glycol flow

The necessary cooling of the engine is achieved through a 50%-50% water-glycol mixture passing through the tubular heat exchanger, which serves as the cooler. Water-Glycol is used as HTF in several applications in industry, due to its altered thermal properties when compared with water. The significant depression of the freezing point compared to water makes this mixture ideal in industrial process cooling applications when temperatures reach minus centigrade. On the other hand, this comes at the cost of reducing the specific heat capacity when compared to water.

2.2.2. Heat exchangers

As mentioned above, both the cooler and the heater are tubular crossflow heat exchangers, with one mixed flow (sodium or water-glycol) and one unmixed flow (working gas).

Although the type of heat exchanger is the same, the fundamental dimensions of the heater and the cooler differ. The bundle of tubes is arranged within the boundaries of a rounded rectangle, with width (W) and height (H), while the components are connected through flanges welded around the rectangular array of tubes. L denotes the total length of the heat exchanger. The tubes are arranged in a triangular lattice, with each tube having 6 equidistant tubes around it. The distance between the centers of tubes is defined as the pitch (p), while the thickness of the tubes (t) and their inner diameter(d) are the only other required dimensions to define the

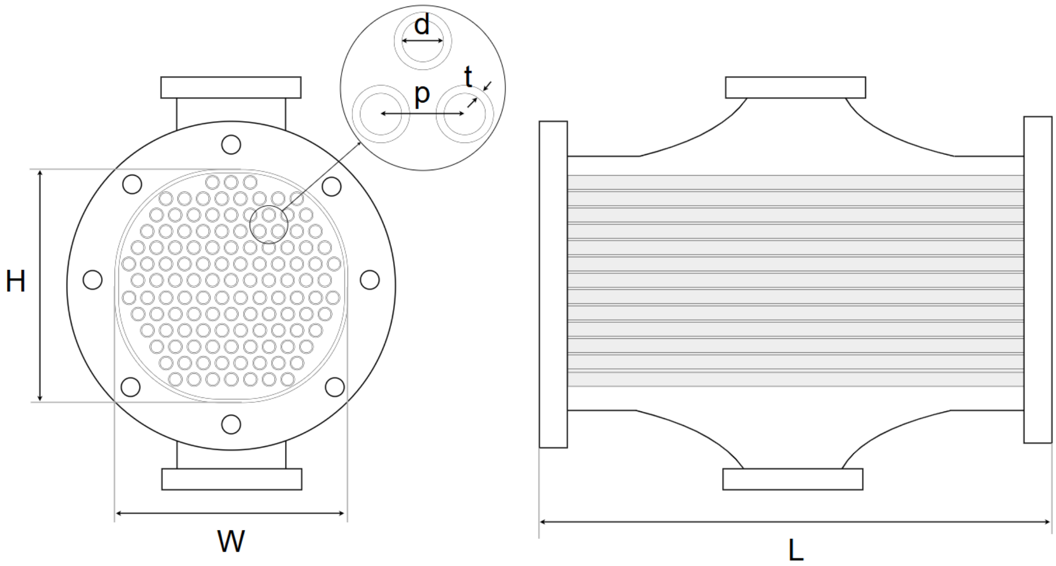

Figure 2.5: Geometric details of the tubular heat exchangers (heater and cooler). The left view shows the arrangement of tubes in a triangular lattice within a rounded rectangular shell, indicating the overall height (H), width (W), tube inner diameter (d), pitch (p), and thickness (t). The right view shows the side profile, indicating the overall length (L).

geometry of the heat exchanger

2.2.3. Regenerator

A fundamental component of the Stirling engine is the regenerator. The regenerator acts as an internal heat exchanger, playing a crucial role in enhancing the efficiency of the Stirling machine. During a cycle, the regenerator stores heat from the working fluid as it passes from the hot to the cold side of the engine. The heat is consequently added to the flow when the working gas flows from the cold to the hot side of the engine. Thus, the role of the regenerator can be characterized as a 'thermal capacitor', significantly reducing the amount of heat that needs to be added and removed from the flow during the phases of the heat addition and rejection, from the external heat reservoirs.

Several types of regenerators have been conceptualized and implemented over the years. Among these, the most widely used are stacked wire screens, random fibers (metal felts), and packed balls. Electron247 utilizes a stacked wire screen regenerator, the most commonly used type of regenerator.

Mesh parameters

The geometrical parameters of the mesh and regenerator are depicted in Figure 2.6.

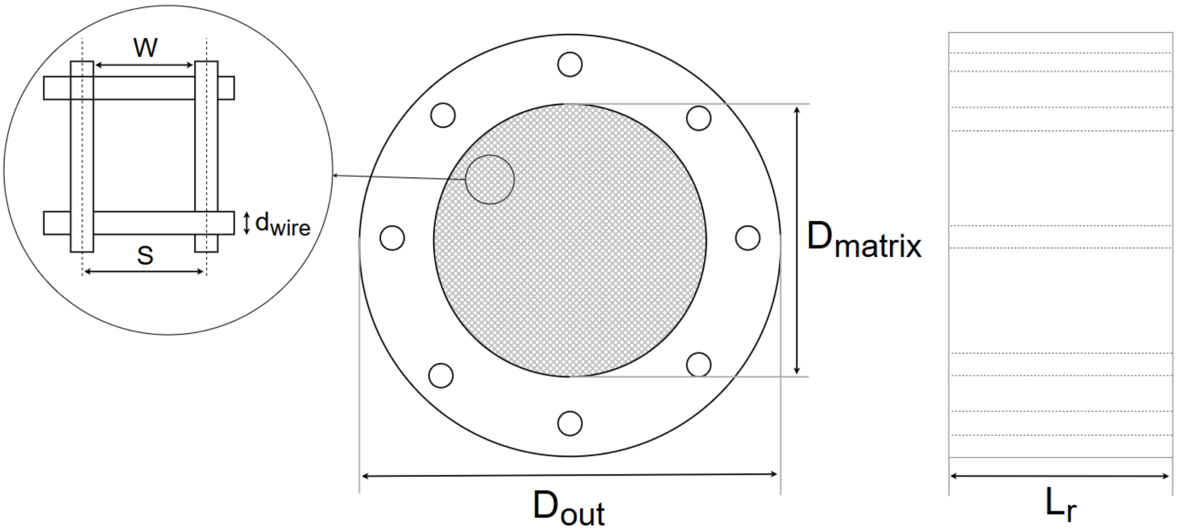

Figure 2.6: Geometrical parameters of woven screen mesh regenerators, the left figure indicates the outer and matrix diameters, with a zoomed-in view for the mesh characteristics. The right figure shows the side profile along with the regenerator length.

The hydraulic diameter, the volumetric porosity, and the velocity in the matrix are defined as:

$$\epsilon = 1 - \frac{V_{matrix}}{V_{total}} \quad (2.2) \qquad d_{hyd} = d_{wire}\frac{\epsilon}{1-\epsilon} \quad (2.3) \qquad u = \frac{u_0}{\epsilon} \quad (2.4)$$

The volume of the matrix is easily defined by the density of the wire material, and the mass of the regenerator $V_{matrix} = m_{reg}/\rho_{wire}$, the total volume of the regenerator is defined as $V_{total} = \frac{\pi}{4}D_r^2$. u_0 is the velocity of the working gas in an empty tube.

2.3. Fundamental modes of heat transfer

The heat transfer rate between two bodies with different and constant temperatures can be obtained with the use of the following formula:

$$Q = \frac{\Delta T}{R} \quad (2.5)$$

where ΔT is the temperature difference and R is the overall thermal resistance between the bodies.

Conduction is the mode of heat transfer that occurs through a stationary medium, which can be a solid, liquid, or gas, as a result of direct molecular interactions driven by a temperature gradient. In the context of heat exchangers, conduction is most significant within the solid materials that constitute the exchanger, particularly through the walls of the tubes that separate the hot and cold fluids. The rate at which heat is transferred by conduction is quantified by Fourier's Law of Heat Conduction [26]:

$$q_k = -kA\frac{dT}{dx} \quad (2.6)$$

Where q_k represents the rate of heat transfer, k is the conductivity, which is a material property, A is the area perpendicular to the direction of the heat flow, and $\frac{dT}{dx}$ is the temperature gradient in the direction of the heat flow.

In a tubular heat exchanger, the conduction equation is applied to calculate the resistance of the wall to thermal heat transfer. The resistance calculation is expressed as:

$$R_w = \frac{ln(d_o/d_i)}{2\pi k_w L} \tag{2.7}$$

Where d_o is the outer diameter of the tube, d_i the inner diameter, k_w the wall thermal conductivity, and L the length of the tube.

Convective heat transfer is the process of thermal energy transfer that occurs at the interface between a moving fluid and a solid surface. It can be further categorized into natural and forced convection. In heat exchangers, forced convection is relevant due to the forced circulation of fluids within the heat exchanger, facilitated by components such as pumps. The rate of heat transfer by convection is described by Newton's law of cooling [26]:

$$q_{conv} = hA(T_s - T_f) \tag{2.8}$$

Where q_{conv} is the rate of heat transfer, h is the convective heat transfer coefficient, $A$is the surface area of the interface between the surface and the fluid, T_s is the bulk area of the solid surface, and T_f is the bulk temperature of the fluid. The resulting resistance due to heat transfer is expressed as:

$$R_{conv} = \frac{1}{hA} \tag{2.9}$$

It is important to mention that this resistance equation is applied twice, once for the internal (tube) flow and once for the external (shell) flow in a tubular heat exchanger.

Radiative heat transfer is described as the energy emitted in the form of electromagnetic waves from any matter that has a temperature above absolute zero. Unlike conduction and convection, radiation does not necessitate a physical medium for its propagation and can therefore occur even through a vacuum. The maximum rate of radiation that can be emitted from an ideal emitter, known as a black body, is described by the Stefan-Boltzmann Law [26]:

$$q_{rad} = \epsilon \sigma A(T_h^4 - T_c^4) \tag{2.10}$$

Where q_{rad} is the radiative heat transfer rate, ϵ is the emissivity of the surface, σ is the Stefan-Boltzmann constant, A is the surface area, T_h is the surface temperature of the hot element, and T_c is the surface area of the cold element.

In the context of typical compact heat exchanger analysis, analysts usually neglect the radiative heat transfer characteristics. The conduction and convection mechanisms of heat transfer are often dominant in such scenarios, and these are typically taken into account when modeling heat exchangers [26].

The overall resistance to heat transfer results in:

$$R_{tot} = \frac{1}{U_o A_o} = \frac{1}{U_i A_i} = \frac{1}{A_i h_i} + \frac{ln(d_o/d_i)}{2\pi k_w L} + \frac{1}{A_o h_o} \tag{2.11}$$

2.4. Thermodynamic modeling of Stirling engines

The ideal cycle of the Stirling engine, as presented in the previous chapter, deviates substantially from the real cycle of a working machine. Over the years, several attempts have been made to model the real cycle of a Stirling machine.

2.4.1. Ideal (Schmidt) analysis - First order

The Ideal Schmidt analysis is a first-order thermodynamic model used to evaluate the performance and cycle of a Stirling machine. It is based on critical simplifying assumptions [17]:

1. The expansion and compression processes in the cycle are isothermal, occurring at constant temperatures due to perfect heat transfer.
2. The working fluid of the engine behaves as an ideal gas at all times, obeying the ideal gas law.
3. There is no friction between the components and the working fluid, resulting in zero pressure loss during the cycle
4. The regenerator is assumed perfect. There is no axial conduction of heat between the cooler and heater through the regenerator. Furthermore, the efficiency of heat recovery through the regenerator is assumed to be 100% with no pressure drop in the regenerator mesh.
5. The volume variations in the expansion and compression spaces are assumed to be sinusoidal functions of the crank angle.

The conceptualization of the Schmidt analysis for a Stirling engine primarily involves applying the conservation of mass equations and the ideal gas law.

$$m = \frac{pV}{RT} \tag{2.12}$$

The work and power approximations are calculated by integrating the pressure over the volume change during the cycle. The Ideal Schmidt Analysis provides a computationally efficient method for estimating theoretical performance.

$$Q_e = \oint p \frac{dV_e}{d\theta} d\theta \tag{2.13}$$

$$Q_c = \oint p \frac{dV_c}{d\theta} d\theta \tag{2.14}$$

$$W = Q_e + Q_c \tag{2.15}$$

Although first-order models perform poorly in approximating the cycle, work, and efficiency of a real machine, this model forms the basis for more accurate models.

2.4.2. Adiabatic models - Second order

Adiabatic models represent a step towards more realistic Stirling engine cycle analysis. The isothermal assumptions during the expansion and compression phases are completely removed. In contrast, these processes are modeled as adiabatic, and the heat rejection and addition occur solely in the heat exchanger components of the machine. The following assumptions hold:

1. The compression and expansion phases take place in adiabatic cylinders, wherein no heat transfer is observed between the working fluid and the cylinder walls.
2. The net heat transfer from and to the external streams occurs exclusively in the heat exchangers.

Adiabatic models incorporate the heat transfer between the working gas and the heat exchangers (heater, cooler, regenerator). Some may also include preliminary estimates of parasitic losses, such as friction and leakage. Specific second-order models account for non-ideal regenerator performance and pressure drops within the engine. These models aim to capture real-world inefficiencies that are often overlooked in idealized analyses. By incorporating heat transfer and loss estimations, adiabatic models offer a more accurate prediction of engine performance.

2.4.3. Quasi-steady models - Third order

Quasi-steady models represent a further refinement in the thermodynamic modeling of Stirling engines by incorporating finite heat transfer rates and flow losses. These models move beyond the ideal heat exchanger assumptions of lower-order models and account for the fact that heat transfer in real engines occurs at a finite rate. They also consider pressure drops that occur due to viscous flow in the heat exchangers and other engine components. Often, these models utilize empirical correlations for heat transfer coefficients and friction factors, derived from experimental data, to improve the accuracy of their predictions. By incorporating these effects, quasi-steady models offer a more accurate representation of the thermodynamic processes within the engine.

A common approach in third-order modeling is nodal analysis, where the engine space is divided into several interconnected one-dimensional nodes or control volumes. The fundamental conservation equations for mass, energy, and momentum are then applied to each of these nodes. The resulting system of differential equations is typically solved numerically for each time step of the engine cycle [15]. This approach allows for the prediction of transient information, such as pressure, temperature, and flow rates, throughout the engine cycle, offering a more detailed understanding of the engine's dynamic behavior. Quasi-steady models generally provide more accurate predictions of engine performance compared to ideal and adiabatic models because they capture non-ideal effects that are neglected in lower-order approaches. Validation of these models against experimental data has shown improved accuracy compared to simpler models. The nodal analysis offers a detailed examination of the spatial and temporal variations in thermodynamic parameters. The ability to predict transient behavior is valuable for analyzing engine start-up and operation under varying conditions.

Urieli and Berchowitz

The adiabatic model published by Urieli and Berchowitz in 1984 [17] is one of the first comprehensive mathematical models to evaluate the performance of a Stirling machine. The same authors also published the so-called 'Simple' model, which includes analysis for imperfect heat exchangers and pressure loss in engine components. These models serve as a basis for future researchers, facilitating the construction of more accurate models.

Babaelahi and Sayyaadi

Babaelahi and Sayyaadi published 'Simple-II' in 2014 [18], modifying the Simple model by Urieli and Berchowitz to enhance its performance. The main additions to the model are the implementation of the working gas leakage effect and non-ideal thermal operation of the regenerator, including longitudinal heat conduction between the heater and cooler through the regenerator. Adding to these, mechanical friction and power loss (based on the theory of finite speed thermodynamics (FST)) due to the piston motion were added. A few years later, the same authors published the polytropic analysis of Stirling engine with various losses (PSVL) [27] and the modified PSVL [28], increasing the prediction efficiency even further, by modeling the polytropic expansion and compression processes.

Table 2.1 features a comparison between the models' results and experimental measurements of the well-established GPU-3 gamma Stirling engine. Analyzing the performance of the models reveals valuable insights for the evolution of the models.

Model (Year)	Heat Input kW (Error (%))	Power kW (Error (%))	η % (Error (%))
Urieli and Berchowitz adiabatic model (1984)	13.280 (+6.8)	8.3 (+213.2)	62.5 (+193.4)
Urieli and Berchowitz simple model (1984)	12.762 (+2.5)	6.7 (+152.8)	52.5 (+146.4)
Hosseinzade and Sayyaadi CAFS model (2014)	11.345 (-8.8)	4.1 (+54.7)	36.2 (+69.9)
Babaelahi and Sayyaadi Simple-II model (2014)	12.746 (+2.4)	3.62 (+36.6)	28.4 (+33.3)
Babaelahi and Sayyaadi PSVL model (2015)	15.450 (+24)	3.03 (+14.3)	24.4 (+14.5)
Babaelahi and Sayyaadi Modified PSVL model (2015)	11.61 (-6.6)	2.87 (+8.3)	24.7 (+15.9)
Experimental results	12.44	2.65	21.3

Table 2.1: Comparison of second-order thermodynamic models against experimental results for the GPU-3 Stirling engine. The table shows the predicted heat input, power output, and thermal efficiency from various models, along with their percentage error relative to the actual experimental data.

Early models: The initial adiabatic and 'simple' models by Urieli and Berchowitz (1984) exhibit significant discrepancies, particularly in their predictions of power output and thermal efficiency, when compared to experimental results. The errors exceed +150% for power and +140% for efficiency, indicating that while foundational, these early models lacked the refinements needed to capture crucial real-world loss mechanisms accurately.

Progressive Improvement: Subsequent models demonstrate a clear trend of improved predictive accuracy, especially for power and efficiency. The inclusion of additional physical effects, such as leakage, non-ideal regenerator operation, longitudinal conduction (Simple-II), and finite speed thermodynamics/polytropic processes (PSVL models), significantly reduces the error margins.

Overall assessment: The table, the prediction for the heat input, the power output, and the thermal efficiency represent a substantial improvement over the years. It is important to note that these results are extracted from comparing the experimental data and modeling results of a gamma Stirling machine. Since alpha engines feature two distinct cylinders, the adiabatic expansion and compression processes modeled in several second-order models are closer to reality when compared to a gamma engine. Adding to this, several engines have the heater and cooler integrated on the wall of the cylinder, directly contradicting the specified assumption (adiabatic compression and expansion). However, the alpha engine of Electron247 features compression and expansion spaces separated from the heater and cooler components, which aligns the adiabatic assumption more closely with the physical system. This suggests that even older, poorly performing models may perform better when simulated using the parameters from EnergyIntel's engine.

2.4.4. Computational fluid dynamics - Fourth, Fifth order

Computational Fluid Dynamics (CFD) models represent the highest level of detail in the thermodynamic analysis of Stirling engines. These models provide detailed two-dimensional or three-dimensional simulations of the fluid flow and heat transfer phenomena within the engine.

CFD simulations can capture complex flow characteristics such as turbulence, recirculation zones, and boundary layer effects, which are often simplified or neglected in lower-order models.
CFD models possess the capability to simulate non-ideal gas behavior, which is particularly important at high operating pressures. Furthermore, CFD allows for a more accurate representation of the regenerator, including its complex geometry and the flow of the working fluid through its porous media. These detailed simulations are invaluable for advanced design and optimization efforts, including parametric studies and the optimization of engine geometry. CFD models can also be used to analyze instabilities and pumping losses within the engine components. While offering the highest level of accuracy and detail, CFD simulations are computationally intensive and require significant computing resources and time. The success of CFD modeling heavily relies on factors such as proper boundary conditions, mesh quality, and convergence of the numerical solution. The multidimensional analysis provided by CFD enables a deep understanding of complex flow and heat transfer. These models are powerful tools for advanced design and optimization, despite their high computational cost.

2.5. Model selection

Selecting an appropriate thermodynamic model for analyzing and optimizing a Stirling engine involves striking a balance between accuracy and computational complexity. As previously discussed, models range from first-order ideal analyses (such as the Schmidt model) to highly detailed fourth- and fifth-order Computational Fluid Dynamics (CFD) simulations.

Considering the goals of this work, which include parametric optimization of engine components, computational efficiency is a critical factor. Optimization algorithms often require numerous iterations of the thermodynamic model to explore the design space. While higher-order models offer greater accuracy, their computational cost can make extensive optimization studies impractical. Third-order models present a compelling compromise. They capture key non-ideal effects neglected by first and second-order analysis, providing sufficiently accurate results for comparative design studies, while remaining computationally tractable for integration within optimization loops.

Additionally, several third-order models are enhanced versions of Urieli and Berchowitz's model, featuring improved loss mechanisms that are not present in the original model. By adapting the initial model to specific engines, it is possible to improve the performance of a model.

Lastly, since 1984, newer correlations have been developed primarily for the heat transfer characteristics of oscillating flows in heat exchangers and regenerators. Implementing these correlations will also improve the predictive performance of the model.

Taking everything into account, a third-order quasi-steady modeling approach, specifically adapted to Electron247's characteristics, is selected for the subsequent analysis and optimization of the Stirling engine.

3

Mathematical and computational model development

The following step in the process is the conceptualization and formulation of the mathematical model that predicts the performance of the Stirling engine. The model simulates the thermodynamic cycle of the engine, from which all the required parameters for evaluating the engine's performance can be extracted.

$$P_{out}, \epsilon_{engine} = f(l_h,\, d_h,\, p_h,\, l_k,\, d_k,\, p_k,\, l_r,\, d_{omat},\, porosity,\, d_{wire})$$

Where heater length l_h, heater inner tube diameter d_h, heater tube pitch p_h, cooler length l_k, cooler inner tube diameter d_k, cooler tube pitch p_k, regenerator length l_r, regenerator matrix outer diameter d_{omat}, regenerator porosity, regenerator wire diameter d_{wire}.

3.1. Geometry generation

The geometry of the heat exchangers is generated based on the dimensional inputs of the model. The primary challenge is to create a triangular lattice based on the pitch and external dimensions of the heat exchanger shells. The algebraic expressions and the methodology behind the geometry generation are explained thoroughly in Appendix B.

3.2. Cycle thermodynamic model

Following, the theoretical procedure behind the system of ordinary differential equations is explained. In practice, the main power output and efficiency of the engine are governed by the tradeoff between pressure drop and effective heat transfer in compact heat exchangers (heater, cooler, regenerator). The theory behind analyzing heat exchangers under steady-state flow conditions is well-established and documented, based on both empirical and analytical models. However, the steady flow conditions do not apply to the working gas in a Stirling engine closed thermodynamic loop, due to the oscillating and flow-reversing conditions. Consequently, the analysis of the thermodynamic cycle is based on the Quasi-steady flow method. This method involves discretizing the engine cycle into small time steps (or crank angle increments) and applying steady-state correlations for heat transfer and fluid friction to the instantaneous conditions at each step. The model is developed based on this fundamental assumption.

The model consists of a main set of ordinary differential equations that predict the system's state based on the given conditions of the previous timestep. Among the several loss mechanisms modeled, some of the losses directly influence the evolution of the differential equations. More specifically, the losses due to the polytropic nature of the thermodynamic process and the heat transfer from the cylinders to the cooling stream are directly incorporated into the set of differential equations. This is depicted in Figure 3.1.

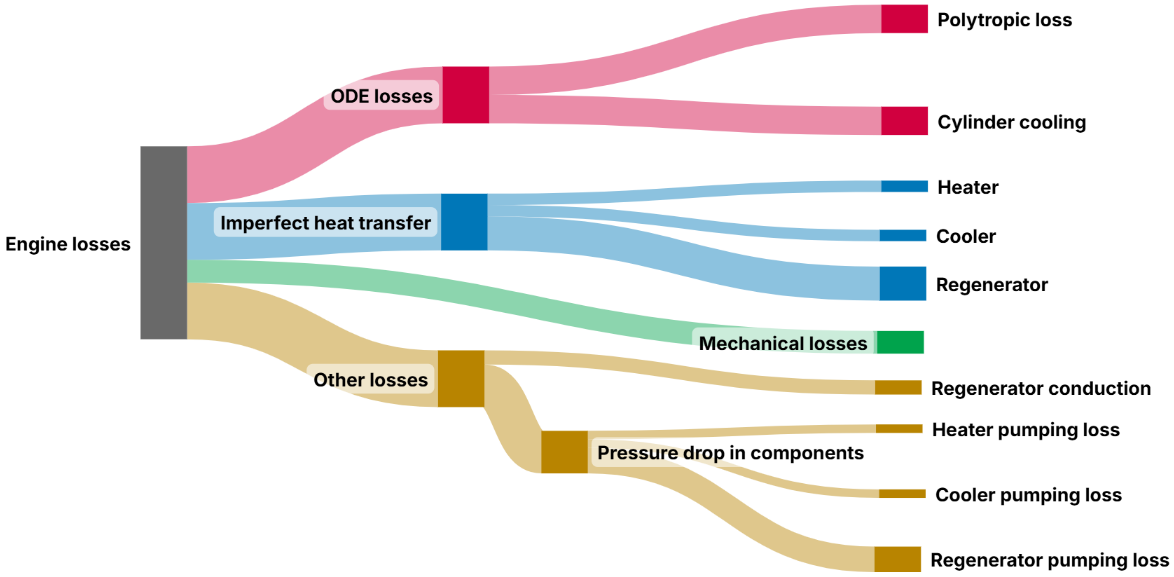

Figure 3.1: Sankey diagram illustrating the different losses implemented in the model. From top to bottom is the chronological order which the losses are computed in the model.

Additionally, the losses due to imperfect heat transfer are calculated after the differential equation has obtained the complete cycle solution. These factors influence the engine's performance. Lastly, the losses due to pressure drop and regenerator conduction are implemented in the model.

3.2.1. Working gas mass

In the thermodynamic modeling of Stirling engines, directly defining the total mass of the working gas (M) is often impractical as it is not a typically known design parameter. The analysis presented by Urieli [17], therefore, adopts a more convenient method where the total mass is not an input but is instead approximated from a more easily specified operational parameter: the mean operating pressure (p_{mean}) of the cycle.

The calculation relies on the results of the Schmidt Analysis, which provides a closed-form solution for an idealized Stirling cycle assuming sinusoidal volume variations and isothermal processes. This analysis yields a direct relationship between the total mass of the working gas, the engine's geometry, its operating temperatures, and the resulting mean cycle pressure. By rearranging the equation for mean pressure derived in the Schmidt analysis, the total mass of the working gas (M) can be calculated as follows:

$$M = \frac{p_{mean} \cdot s \cdot \sqrt{1-b^2}}{R} \tag{3.1}$$

where:

- p_{mean} is the specified mean charge pressure of the engine.

- R is the specific gas constant of the working fluid.
- s is a summation term representing the total equivalent volume of the engine, normalized by temperature. It is calculated as:

$$s = \left[\frac{V_{swc}}{2T_k} + \frac{V_{clc}}{T_k} + \frac{V_k}{T_k} + \frac{V_r}{T_r} + \frac{V_h}{T_h} + \frac{V_{swe}}{2T_h} + \frac{V_{cle}}{T_h}\right]$$

- b is a dimensionless parameter related to the pressure variation, calculated as c/s, where c is a term representing the combined effect of the swept volumes and their phase angle, normalized by temperature.
- $\sqrt{1-b^2}$ is a term that accounts for the sinusoidal nature of the pressure variation.

This method provides a robust and practical way to initialize the simulation with a realistic quantity of working gas based on a primary, controllable operating condition (p_{mean}), rather than requiring the less intuitive direct specification of mass.

3.2.2. Development of system of ODEs

The development of the system of ODEs is based on the Simple model for Stirling engine cycle analysis from I. Urieli [17] and the Modified Polytropic model for Stirling analysis with various losses from Babaelahi et al. [28]. This model solves a system of ordinary differential equations to determine the pressure of the engine and the corresponding temperatures for each engine compartment. After the solution of the system of equations is obtained, an analysis is performed to determine the irreversibilities of the engine due to imperfect heat transfer and fluid friction pressure drops.

The model discretizes the total engine volume into five interconnected control volumes: compression space (c), cooler (k), regenerator(r), heater (h), and expansion space (e) (Figure 3.2).

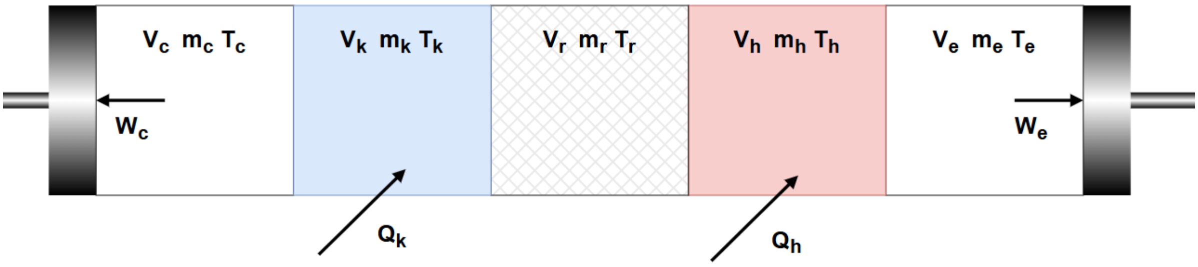

Figure 3.2: The five distinct compartments of the engine, namely, compression space (c), cooler (k), regenerator (r), heater(h), and expansion space (e).

The five distinct engine compartments are connected in series. The cycle is divided into 360 different crank angle increments, one for every angle of rotation of the engine's crankshaft. A key assumption in this model is that at any given crank angle, the temperature within each control volume is spatially uniform. However, the temperatures of the compression (T$_c$) and expansion (T$_e$) volumes vary dynamically throughout the cycle, as shown in Figure 3.3. The temperatures of the heater and cooler are dependent on both the thermodynamic cycle and the inlet temperatures of the heat transfer fluids. They are calculated iteratively until convergence. The pressure of the engine is considered uniform over the five compartments.

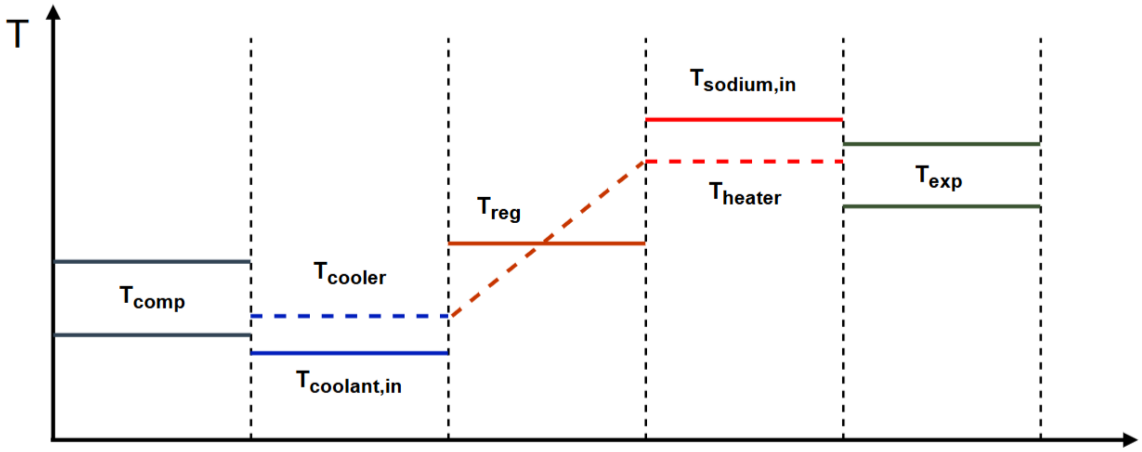

Figure 3.3: The assumed temperature distributions over the 5 distinct engine compartments.

The temperature distribution of the regenerator is considered linear and is evaluated based on Equation 3.2.

$$T_{\text{regenerator}} = \frac{T_{\text{heater}} - T_{\text{cooler}}}{ln(T_{\text{heater}}/T_{\text{cooler}})} \tag{3.2}$$

Polytropic indices

Due to the polytropic nature of the model, the state of the compression and the expansion spaces can be modeled obeying Equation 3.3.

$$pV^n = \text{constant} \tag{3.3}$$

The polytropic indices for the compression and expansion spaces can be obtained by differentiating Equation 3.3 and solving for n.

$$n_e = -\frac{V_e dP}{p dV_e} \qquad n_c = -\frac{V_c dP}{p dV_c} \tag{3.4}$$

Equation of state

Moving on to defining the system of differential equations, it is assumed that the working gas follows ideal gas behavior. This assumption is based on the fact that the engine always operates away from the critical point of the working gas. For reference, the critical point of hydrogen is at 33.2 K and 12.0 bar, while that of helium is 5.2 K and 2.26 bar. As a result, the ideal gas law can be used as the equation of state (Equation 3.5).

$$pV = mRT \tag{3.5}$$

Neglecting the gas leakage effects through the piston seals, the mass of the working gas is assumed to be constant and equal to:

$$m_c + m_k + m_r + m_h + m_e = M \tag{3.6}$$

Combining the mass conservation, its derivative, and the state equation, the following equation is obtained

$$\frac{dm_c}{d\theta} + \frac{dm_e}{d\theta} + \frac{dp}{d\theta}\frac{1}{R}(\frac{V_k}{T_k} + \frac{V_r}{T_r} + \frac{V_h}{T_h}) = 0 \tag{3.7}$$

The volumes and temperatures of the three heat exchangers are constant and known. The goal is to obtain the equations for m_c and m_e to determine an explicit equation for the pressure differential. These can be done by specifying the energy equation for the compression and expansion spaces. This can be done by employing energy conservation relations.

Energy equation

The generalized system of equations is derived by applying the principle of energy conservation to the five control volumes. The generalized control volume is depicted in Figure 3.4a:

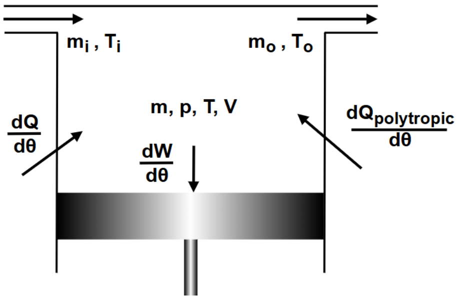

(a) A generalized control volume showing heat, work, and mass-energy transfer terms.

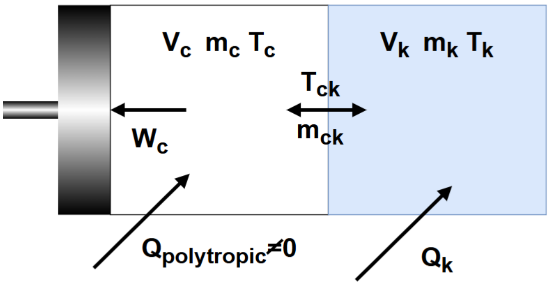

(b) Specific application to the interface between the compression space (c) and the cooler (k).

The derived energy conservation equation equals:

$$\frac{dQ}{d\theta} - \frac{dQ_{\text{polytropic}}}{d\theta} + c_p T_i m_i - c_p T_o m_o = \frac{dW}{d\theta} + c_v \frac{d(mT)}{d\theta} \tag{3.8}$$

Where:

- c_v and c_p are the constant volume and constant pressure-specific heat capacities, respectively.
- $T_{i,o}$, and $m_{i,o}$ are the input and output temperature of the flows in the cell, and the corresponding mass.
- It is assumed that the difference in velocity and altitude between input and output flows are negligible; thus, the kinetic and potential energy terms usually included in the energy equation are neglected.

The double-indexed variables T_{ck} and m_{ck} correspond to the temperatures at and the mass flows through the interfaces between control volumes. These are defined on every interface and simulate the oscillating nature of the working gas in the engine. The temperatures of these interfaces depend on the direction of the flow, being equal to the temperature of the adjacent control volume. The following relations are used to define these:

$$\text{T}_{\text{ck}} = \begin{cases} T_c, & \dot{m}_{\text{ck}} > 0 \\ T_k, & \dot{m}_{\text{ck}} < 0 \end{cases} \qquad \text{T}_{\text{he}} = \begin{cases} T_h, & \dot{m}_{\text{he}} > 0 \\ T_e, & \dot{m}_{\text{he}} < 0 \end{cases}$$

The heat addition and work terms are defined differently for each control volume. Compared to Urieli's model, an additional term is added ($\frac{Q_{\text{polytropic}}}{d\theta}$). This term represents the heat transfer between the working gas and the cylinder walls in the compression and expansion volumes, as well as the deviation of the process from the adiabatic case. This heat transfer causes the processes to deviate from the ideal adiabatic condition, becoming polytropic. The calculation of the polytropic loss factor in the energy equation requires taking into account both the thermodynamic nature of the processes and the heat transfer characteristics inside and outside of the expansion and compression cylinders. The heat transfer from the internal flow to the external cooling flow can be approximated by Equation 3.9.

$$\dot{Q}_{\text{cooling}} = \frac{T - T_{\text{cooling}}}{R_t} \tag{3.9}$$

Where:

- T_{cooling} is the average temperature of the cooling flow
- $R_t = \frac{1}{A_i h_i} + \frac{ln(d_o/d_i)}{2\pi k_w L} + \frac{1}{A_o h_o}$ is the total thermal resistance between the cooling flow and the working gas. In this equation, the A_i, A_o, and h_i, h_o are the inner and outer heat transfer areas and convective heat transfer coefficients, k_w is the thermal conductivity of the wall, d_o and d_i are the outer and inner diameters of the cylinder. L is the height of the cylinder.

The polytropic process heat loss is defined in Equation 3.10

$$Q_{\text{polytropic}} = mC_n \left(\frac{R_{\text{conv,i}}}{R_t} \right) (T - T_{\text{cooling}}) \tag{3.10}$$

Where:

- $C_n = c_v \frac{n-k}{n-1}$ is the polytropic specific heat
- $R_{\text{conv,i}} = \frac{1}{A_i h_i}$ is the thermal resistance between the working gas and the cylinder.

Substituting these equations in the general energy conservation equation and simplifying results in the compression space mass differential (Equation 3.11).

$$\frac{dm_c}{d\theta} = \frac{\frac{p}{RT_{ck}} \frac{dV_c}{d\theta} + \frac{V_c}{R\gamma T_{ck}} \frac{dp}{d\theta} + \left(\frac{m_c C_{nc} R_{\text{conv,i}}}{c_p T_{ck} R_t} \right) \frac{dT_c}{d\theta}}{1 + \left(\frac{C_{nc} R_{\text{conv,i}}}{c_p T_{ck} R_t} \right) (T_{\text{cooling}} - T_c)} \tag{3.11}$$

Similarly, the mass differential for the expansion space can be obtained.

The boundary conditions are derived from the mass balance, $dm_c = m_{ck}$ and $m_{rh} = m_{he} - dm_h$. Substituting these in the expression of differential pressure and solving for pressure, the full expression is obtained.

$$\frac{dp}{d\theta} = - \frac{\dfrac{\frac{p}{T_{ck}} \frac{dV_c}{d\theta} + R \left(\frac{m_c C_{nc} R_{\text{conv,i}}}{c_p T_{ck} R_t} \right) \frac{dT_c}{d\theta}}{1 + \left(\frac{C_{nc} R_{\text{conv,i}}}{c_p T_{ck} R_t} \right) (T_{\text{cooling}} - T_c)} + \dfrac{\frac{p}{T_{he}} \frac{dV_e}{d\theta} + R \left(\frac{m_e C_{ne} R_{\text{conv,i}}}{c_p T_{he} R_t} \right) \frac{dT_e}{d\theta}}{1 + \left(\frac{C_{ne} R_{\text{conv,i}}}{c_p T_{he} R_t} \right) (T_{\text{cooling}} - T_e)}}{\dfrac{\frac{V_c}{\gamma T_{ck}}}{1 + \left(\frac{C_{nc} R_{\text{conv,i}}}{c_p T_{ck} R_t} \right) (T_{\text{cooling}} - T_c)} + \dfrac{\frac{V_e}{\gamma T_{he}}}{1 + \left(\frac{C_{ne} R_{\text{conv,i}}}{c_p T_{he} R_t} \right) (T_{\text{cooling}} - T_e)} + \left(\frac{V_k}{T_k} + \frac{V_r}{T_r} + \frac{V_h}{T_h} \right)} \tag{3.12}$$

The temperature differentials for compression and expansion space are obtained by rearranging the derivative of the ideal gas law.

$$\frac{dT_c}{d\theta} = T_c \left(\frac{dp}{d\theta} \frac{1}{p} + \frac{dV_c}{d\theta} \frac{1}{V_c} - \frac{dm_c}{d\theta} \frac{1}{m_c} \right) \tag{3.13}$$

$$\frac{dT_e}{d\theta} = T_e \left(\frac{dp}{d\theta} \frac{1}{p} + \frac{dV_e}{d\theta} \frac{1}{V_e} - \frac{dm_e}{d\theta} \frac{1}{m_e} \right) \tag{3.14}$$

The differentials of the heat transfer in the heat exchangers are also obtained by applying the energy conservation equation.

$$\frac{dQ_k}{d\theta} = \frac{V_k c_v}{R} \frac{dp}{d\theta} - c_p (T_{ck} m_{ck} - T_{kr} m_{kr}) \tag{3.15}$$

$$\frac{dQ_r}{d\theta} = \frac{V_r c_v}{R}\frac{dp}{d\theta} - c_p\left(T_{kr}m_{kr} - T_{rh}m_h\right) \tag{3.16}$$

$$\frac{dQ_h}{d\theta} = \frac{V_h c_v}{R}\frac{dp}{d\theta} - c_p\left(T_{rh}m_{rh} - T_{he}m_{he}\right) \tag{3.17}$$

Finally, the total work can be computed along with the distinct compression and expansion piston contributions (Equation 3.18 and Equation 3.19)

$$\frac{dW_c}{d\theta} = p\frac{dV_c}{d\theta} \tag{3.18}$$

$$\frac{dW_e}{d\theta} = p\frac{dV_e}{d\theta} \tag{3.19}$$

An overview of the complete set of equations can be observed in Table 3.1, while the detailed derivation of the model can be found in Appendix C.

Equation	Quantity
$n_e = -\frac{V_e\, dP}{p\, dV_e}, \quad n_c = -\frac{V_c\, dP}{p\, dV_c}$	**Polytropic indexes**
$p = \dfrac{MR}{\frac{V_c}{T_c} + \frac{V_k}{T_k} + \frac{V_r}{T_r} + \frac{V_h}{T_h} + \frac{V_e}{T_e}}$	**Pressure**
$\dfrac{dp}{d\theta} = -\dfrac{\frac{\frac{p}{T_{ck}}\frac{dV_c}{d\theta} + R\left(\frac{m_c C_{nc} R_{\text{conv,i}}}{c_p T_{ck} R_t}\right)\frac{dT_c}{d\theta}}{1+\left(\frac{C_{nc} R_{\text{conv,i}}}{c_p T_{ck} R_t}\right)(T_{\text{cooling}} - T_c)} + \frac{\frac{p}{T_{he}}\frac{dV_e}{d\theta} + R\left(\frac{m_e C_{ne} R_{\text{conv,i}}}{c_p T_{he} R_t}\right)\frac{dT_e}{d\theta}}{1+\left(\frac{C_{ne} R_{\text{conv,i}}}{c_p T_{he} R_t}\right)(T_{\text{cooling}} - T_e)}}{\frac{\frac{V_c}{\gamma T_{ck}}}{1+\left(\frac{C_{nc} R_{\text{conv,i}}}{c_p T_{ck} R_t}\right)(T_{\text{cooling}} - T_c)} + \frac{\frac{V_e}{\gamma T_{he}}}{1+\left(\frac{C_{ne} R_{\text{conv,i}}}{c_p T_{he} R_t}\right)(T_{\text{cooling}} - T_e)} + \left(\frac{V_k}{T_k} + \frac{V_r}{T_r} + \frac{V_h}{T_h}\right)}$	**Pressure Variation**
$m_i = \dfrac{pV_i}{RT_i}, \quad i = c, k, r, h, e$	**Mass**
$\dfrac{dm_e}{d\theta} = \dfrac{\frac{p}{RT_{he}}\frac{dV_e}{d\theta} + \frac{V_e}{R\gamma T_{he}}\frac{dp}{d\theta} + \left(\frac{m_e C_{ne} R_{\text{conv,i}}}{c_p T_{he} R_t}\right)\frac{dT_e}{d\theta}}{1 + \left(\frac{C_{ne} R_{\text{conv,i}}}{c_p T_{he} R_t}\right)(T_{\text{cooling}} - T_e)}$	
$\dfrac{dm_c}{d\theta} = \dfrac{\frac{p}{RT_{ck}}\frac{dV_c}{d\theta} + \frac{V_c}{R\gamma T_{ck}}\frac{dp}{d\theta} + \left(\frac{m_c C_{nc} R_{\text{conv,i}}}{c_p T_{ck} R_t}\right)\frac{dT_c}{d\theta}}{1 + \left(\frac{C_{nc} R_{\text{conv,i}}}{c_p T_{ck} R_t}\right)(T_{\text{cooling}} - T_c)}$	
$\frac{dm_i}{d\theta} = m_i \frac{dP}{d\theta}\frac{1}{P}, \quad i = k, r, h$	
$T_{ck} = \begin{cases} T_c & \text{for } \dot{m}_{ck} > 0 \\ T_k & \text{else} \end{cases}, \quad T_{he} = \begin{cases} T_h & \text{for } \dot{m}_{he} > 0 \\ T_e & \text{else} \end{cases}$	**Conditional temperatures**
$\frac{dT_c}{d\theta} = T_c\left(\frac{dp}{d\theta}\frac{1}{p} + \frac{dV_c}{d\theta}\frac{1}{V_c} - \frac{dm_c}{d\theta}\frac{1}{m_c}\right)$	**Temperature variation**
$\frac{dT_e}{d\theta} = T_e\left(\frac{dp}{d\theta}\frac{1}{p} + \frac{dV_e}{d\theta}\frac{1}{V_e} - \frac{dm_e}{d\theta}\frac{1}{m_e}\right)$	
$\frac{dQ_k}{d\theta} = \frac{V_k c_v}{R}\frac{dp}{d\theta} - c_p\left(T_{ck} m_{ck} - T_{kr} m_{kr}\right)$	**Heat output of cooler**
$\frac{dQ_r}{d\theta} = \frac{V_r c_v}{R}\frac{dp}{d\theta} - c_p\left(T_{kr} m_{kr} - T_{rh} m_h\right)$	**Heat exchange in regenerator**
$\frac{dQ_h}{d\theta} = \frac{V_h c_v}{R}\frac{dp}{d\theta} - c_p\left(T_{rh} m_{rh} - T_{he} m_{he}\right)$	**Heat input to heater**
$\frac{dW_c}{d\theta} = p\frac{dV_c}{d\theta}$	
$\frac{dW_e}{d\theta} = p\frac{dV_e}{d\theta}$	**Work in compression/expansion**

Table 3.1: ODE system of the cycle thermodynamic model.

3.3. Additional losses

After the set of ordinary differential equations is defined, additional loss mechanisms are implemented. The imperfect heat transfer phenomena in heat exchangers significantly influence the overall performance of the engine, playing a crucial role in the model's predictive efficiency. Additionally, conduction losses through the regenerator are also modeled. Lastly, the pressure drop in the components due to fluid friction is implemented; this is crucial because the pressure drop in the engine directly influences the work output. In a way, the piston movement needs to counteract the work due to the pressure drop, which is directly subtracted from the work output.

3.3.1. Imperfect heat transfer in heat exchangers

A fundamental assumption of the thermodynamic model is that the heater and the cooler have uniform temperatures. In reality, the inlet and outlet temperatures of the sodium and water glycol flows are different. This assumption is based on the fact that the oscillating and reversing flow in the heat exchangers disables the validity of the number of transfer units method, with which the efficiency of a heat exchanger can be approximated with:

$$\epsilon = 1 - e^{NTU} \tag{3.20}$$

However, the temperature difference between the heat transfer fluids and the working gas in the engine can be approximated iteratively by the following equations:

$$T_k = T_{water} - \frac{Q_k}{R_{tot,k}} \tag{3.21}$$

$$T_h = T_{sodium} - \frac{Q_h}{R_{tot,h}} \tag{3.22}$$

These equations only hold because the temperature differentials between sodium and the working gas, and water-glycol and the working gas, are considered uniform. The total resistances between the two fluids are approximated as:

$$R_{tot,heater} = \frac{1}{h_{sodium} A_{wh,out}} + \frac{ln(d_{h,out}/d_{h,in})}{2\pi k_{ss} L_h N_{tubes,h}} + \frac{1}{h_{gas} A_{wh,in}} \tag{3.23}$$

$$R_{tot,cooler} = \frac{1}{h_{\text{cooler}} A_{wk,out}} + \frac{ln(d_{k,out}/d_{k.in})}{2\pi k_{ss} L_k N_{tubes,k}} + \frac{1}{h_{gas} A_{wk,in}} \tag{3.24}$$

Where:

- $A_{wk,out} = N_{tubes,k} \pi d_{k,out} L_k$ and $A_{wh,out} = N_{tubes,h} \pi d_{h,out} L_h$ correspond to the wetted outer areas of tubes for heater and cooler
- $A_{wk,in} = N_{tubes,k} \pi d_{k,in} L_k$ and $A_{wh,in} = N_{tubes,h} \pi d_{h,in} L_h$ correspond to the wetted inner areas of tubes for heater and cooler
- L_h, L_k the lengths of heater and cooler, respectively
- k_{kss} the thermal conductivity of stainless steel
- d_{out}, d_{in} the outer and inner diameters of the tubes
- N_{tubes} is the number of tubes

Convective heat transfer coefficients

Calculating the total thermal resistance of heat exchangers requires approximating the convective heat transfer coefficients of the heat-interchanging flows. This is achieved by correlating the Nusselt dimensionless group (Nu).

$$Nu_{s,w,wg} = \frac{h_{s,w,wg} d_{hydraulic}}{k_{s,w,wg}} \tag{3.25}$$

The s,w, and wg subscripts correspond to sodium, water-glycol mixture, and working gas. Different correlations are used for each flow due to different flow characteristics.

Heat transfer fluids

Calculating the heat transfer coefficients of heat transfer fluids requires calculating the fluid velocity at the outer surface of the tubes. The procedure followed for obtaining the velocities is explained in Appendix B.

Sodium

The heat transfer characteristics of sodium were approximated by the Nusselt correlation proposed by Friedland and Bonilla [22] (Equation 3.26), particularly for liquid metal flows across banks of tubes.

$$Nu = 7.0 + 3.8x^{1.52} + 0.027x^{0.27}(Pe)^{0.8} \tag{3.26}$$

Water glycol

Water-glycol flow Nusselt number can be approximated by the correlation derived specifically for heat transfer in banks of tubes by A.P. Colburn [29] (Equation 3.27).

$$Nu = 0.33(Re^{0.6})(Pr^{1/3}) \tag{3.27}$$

Working gas

The Nusselt number of the oscillating flow of the working gas can be approximated by the correlation proposed by Gnielinski [30] and later refined by De Monte et al. [31] (Equation 3.28).

$$Nu = -0.494 + 0.0777\left(\frac{A_R}{1+A_R}\right)^2 Re^{0.7} - 0.00162Re^{0.4}(4Re_\omega)^{0.8} \tag{3.28}$$

where Re_w is defined as the dimensionless oscillation frequency and A_R the oscillation amplitude:

$$A_R = \frac{d\,Re}{l\,Re_w} \qquad Re_w = \frac{\rho_{gas}\omega d^2}{4\mu_{gas}}$$

3.3.2. Heat transfer in the regenerator

The performance of a Stirling engine is heavily dependent on the effectiveness of the regenerator. The effectiveness ϵ of a regenerator is defined as the following ratio:

$$\epsilon = \frac{\text{amount of heat transferred from regenerator to gas}}{\begin{array}{c}\text{equivalent amount of heat transferred from regenerator}\\ \text{to gas under Adiabatic conditions}\end{array}} \tag{3.29}$$

In terms of quantities, the efficiency of the regenerator can be evaluated with Equation 3.30.

$$\epsilon = \frac{1}{\left(1 + \frac{2\Delta T}{T_{h,in} - T_{h,out}}\right)} \tag{3.30}$$

Where ΔT is the temperature difference between the gas stream and the regenerator matrix. $T_{h,in}$ and $T_{h,out}$ are gas inlet and outlet temperatures while the regenerator is in heating mode. Following, the energy balance of the hot stream is defined (Equation 3.31).

$$\dot{Q}_{hot} = c_p\dot{m}(T_{h,in} - T_{h,out}) = 2h_{conv}A_{wg}\Delta T \tag{3.31}$$

Where h_{conv} is the convective heat transfer coefficient of the matrix, and A_{wg} is the wetted area of the regenerator. Substituting the energy equation in the effectiveness equation:

$$\epsilon = \frac{1}{\left(1 + \frac{c_p\dot{m}}{h_{conv}A_{wg}}\right)} = \frac{NTU}{1+NTU} \qquad (NTU = \frac{h_{conv}A_{wg}}{c_p\dot{m}}) \tag{3.32}$$

Through dimensional analysis [17], the number of transfer units in the regenerator is defined (Equation 3.33).

$$NTU = St\frac{A_{wg}}{A} \tag{3.33}$$

Where St is the Stanton number, and A is the flow cross-sectional area. The Stanton number can be approximated by

$$St = \frac{Nu}{RePr} \tag{3.34}$$

While the Nusselt dimensionless number is defined by the correlation (Equation 3.35) resulting from CFD simulations from Costa et al. [32].

$$Nu = 1.14 + 0.39Re^{0.66} \tag{3.35}$$

When the efficiency of the regenerator equals 1, it indicates complete heat recovery. The heat that is not recovered from the regenerator must be supplied by an external heat source (in this case, sodium) through the heater. This results in equations that approximate the non-ideal heat transfer for the heater and the cooler (Equation 3.36 and Equation 3.37).

$$Q_h = Q_{h,ideal} + Q_{r,ideal}(1 - \epsilon) \tag{3.36}$$

$$Q_k = Q_{k,ideal} - Q_{r,ideal}(1 - \epsilon) \tag{3.37}$$

Substituting these in Equation 3.21 and Equation 3.22 for the new cooler and heater temperatures results in Equation 3.38 and Equation 3.39.

$$T_h = T_{sodium} - \frac{(Q_{h,ideal} + Q_{r,ideal}(1 - \epsilon))}{R_{tot,heater}} \tag{3.38}$$

$$T_k = T_{water} - \frac{(Q_{k,ideal} - Q_{r,ideal}(1 - \epsilon))}{R_{tot,cooler}} \tag{3.39}$$

With these equations, the model for the losses due to non-ideal heat transfer in heat exchangers is completed.

3.3.3. Conduction losses through regenerator

In every Stirling engine configuration, the regenerator serves as the connecting component between the cold and hot sides of the engine. Since a temperature differential exists, the solid material of the regenerator conducts thermal energy from the hot to the cold side of the engine, thus increasing the irreversibility of the cycle. This amount of heat can be approximated with the Equation 3.40:

$$Q_{\text{conduction, r}} = R_{\text{conduction, r}}(T_{wh} - T_{wk}) \tag{3.40}$$

Where $R_{\text{conduction, r}} = \frac{k_r a_{wr}}{l_r}$ is the thermal conduction resistance of the regenerator, k_r is the material thermal conductivity, a_{wr} is the heat transfer area through the wall and l_r is the length of the regenerator.

3.3.4. Pressure drop due to fluid friction

Tubular heat exchangers

The model for the pressure drop due to friction in heat exchangers is generally based on the assumption of quasi-steady flow. Equation 3.41 is developed under the defined assumptions, taking into account the oscillatory nature of the flow [17].

$$\Delta p = \frac{-2\mu u C_{ref} V}{d^2 A} \tag{3.41}$$

$C_{ref} = ReC_f$, the Reynolds friction coefficient is obtained from the dimensional analysis of the flow characteristics. The friction coefficient of the flow is obtained from Equation 3.42 and

Equation 3.43, derived by Paul D. Roach and Kenneth J. Bell from experimental measurements of oscillating flows [33]

$$C_{f,cooler} = 0.0778Re^{-0.201} \tag{3.42}$$

$$C_{f,heater} = 0.0265Re^{-0.249} \tag{3.43}$$

Regenerator
Equation 3.44 characterizes the pressure drop along the regenerator.

$$\Delta p = C_f \frac{\rho}{2} \frac{L}{d_h} u^2 \tag{3.44}$$

The friction factor of the regenerator matrix is defined by the correlation developed by experimental measurements by Gedeon and Wood [34].

$$C_f = 129/R_e + 2.91R_e^{-0.103} \tag{3.45}$$

The correlation is validated by the authors to accurately predict the friction factor for $Re = 0.45 - 6100$, porosity$= 0.623 - 0.781$, and d$_{wire} = 80 - 110\mu m$

Finally, the total work loss due to fluid friction in heat exchangers can be obtained through numerical integration with Equation 3.46.

$$W_{\text{loss}} = \int_{\theta=0^\circ}^{\theta=360^\circ} \sum_{i=k,r,h} \Delta P_i dV_e = \int_{\theta=0^\circ}^{\theta=360^\circ} \left(\sum_{i=k,r,h} \Delta P_i \frac{dV_e}{d\theta} \right) d\theta \tag{3.46}$$

3.4. Mechanical friction in engine components

The final loss mechanism modeled in the engine corresponds to the mechanical friction between components, primarily between the cylinder walls and the expansion and compression pistons. This loss can be approximated with the following equation [35]:

$$\Delta p_{friction} = (0.97 + 0.15\frac{RPM}{1000}) \times 10^5 \tag{3.47}$$

The total loss due to mechanical friction can be calculated by integrating the pressure drop over the complete cycle

$$W_{\text{loss}} = \int_{\theta=0^\circ}^{\theta=360^\circ} \Delta p_{friction} \frac{dV}{d\theta} d\theta \tag{3.48}$$

3.5. Solution method

Due to the non-linear and coupled nature of the system of ODEs in the model, a numerical solver must be integrated to solve this. The classic fourth-order Runge-Kutta method is employed.

The algorithm starts by defining the operational parameters and the geometries of the heater, the cooler, and the regenerator. The inlet temperatures of the sodium and the water-glycol are constant, and they are considered system variables. Since the temperatures of the heater and the cooler are assumed constant in the model, they are approximated as the mean of the inlet and outlet temperatures:

$$T_{heater,cooler} = \frac{1}{2}(T_{h,c(in)} - T_{h,c(out)})$$

The outlet temperature of the heater and the cooler are not initially known; thus, for the first iteration, they are set equal to the inlet temperatures.

The set of seven interconnected ODEs (T_c, T_e, Q_k, Q_r, Q_h, W_c, W_e) is treated as an initial value problem. This means that for an initial set of values for $\theta = 0$, the method calculates the state of the system for the next increment of the cycle. The set of 7 ODEs is approximated using the RK4 numerical method, while the remaining variables are determined analytically.

In reality, this is a boundary condition, not an initial value problem, since the actual state at the beginning of the thermodynamic cycle is unknown. However, this is tackled by iteratively solving the system until convergence of the initial and the final values of the problem. This is possible due to the cyclic nature of the thermodynamic process. More particularly, the system of equations is solved for a complete crankshaft rotation ($\theta = 0$ to $\theta = 360$), and until convergence, the end values of the previous iteration are substituted as the initial values for the next one.

Once this inner loop converges, the losses due to imperfect heat transfer in the regenerator, cooler, and heater are determined by Equation 3.32, Equation 3.39, and Equation 3.38, respectively. This process is repeated until the gas temperatures in the three heat exchangers converge.

After convergence of the second loop, the fluid friction pressure drop, regenerator conduction, and the heat exchange of the heater and cooler (Q_h and Q_c) are calculated. With these, the new outlet temperatures for the heater and the cooler can be approximated (Equation 3.49, Equation 3.50). This process is repeated until the outlet temperatures of the tubular heat exchangers converge.

$$T_{h,out} = T_{h,in} - \frac{Q_h}{\dot{m}_{sodium} c_{p,sodium}} \tag{3.49}$$

$$T_{c,out} = T_{c,in} + \frac{Q_c}{\dot{m}_{cool} c_{p,cool}} \tag{3.50}$$

The main logic explained behind the solution can be observed in the following logic diagram:

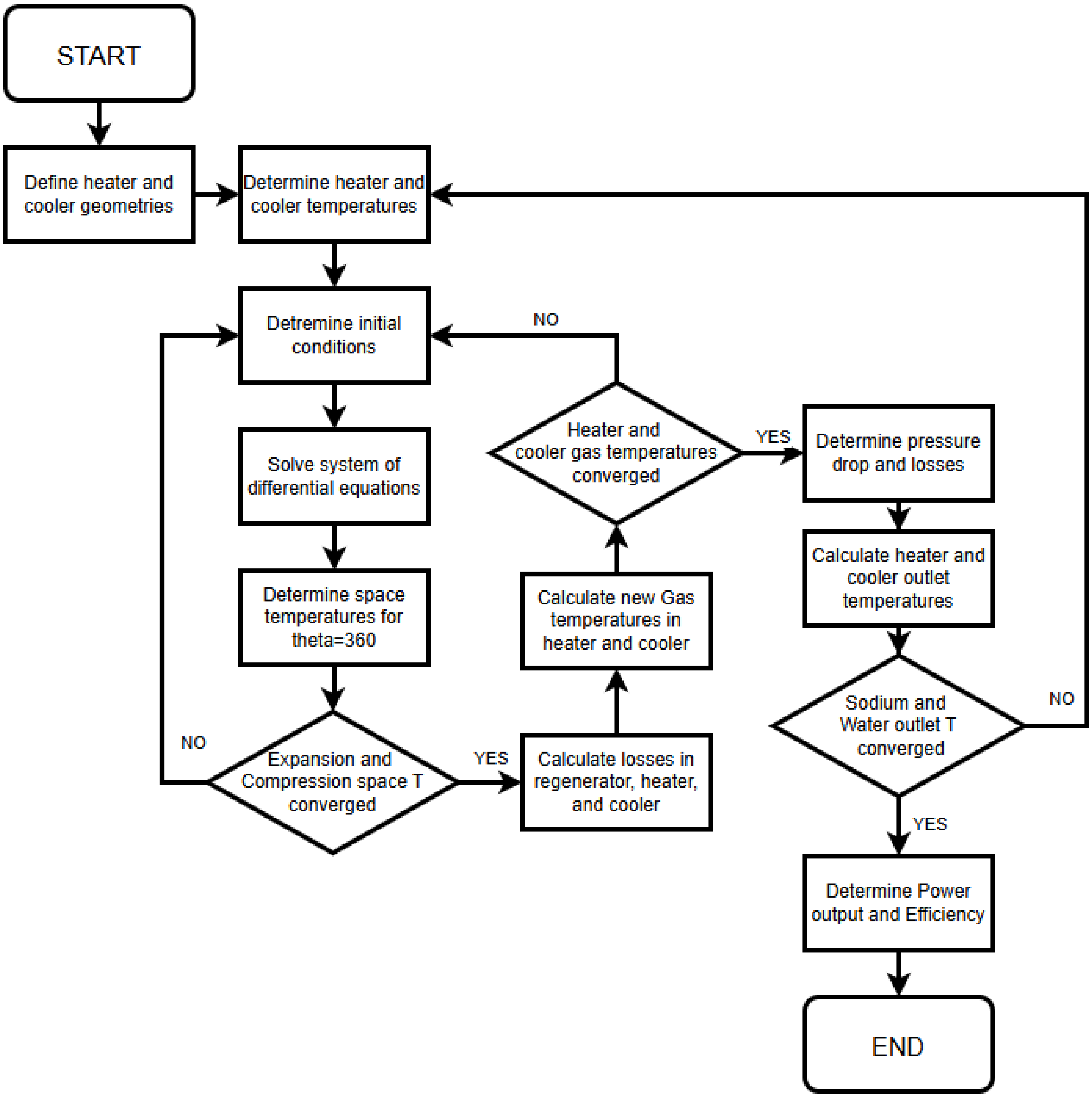

Figure 3.5: Flowchart of the numerical solution method. The diagram illustrates the nested iterative loops required to solve the system of Ordinary Differential Equations (ODEs) for the thermodynamic cycle. It includes an inner loop for cycle convergence, a middle loop for calculating heat exchanger performance and losses, and an outer loop for converging the outlet temperatures of the sodium and water-glycol streams.

3.5.1. Solving implications

Solving the system of ODEs for obtaining a complete cycle solution numerically, two variables are introduced: the polytropic indices. These variables vary with respect to the crank angle; thus, they are determined numerically for each step of the thermodynamic cycle. The rest of the solution is identical to the enhanced adiabatic model.

However, when attempting to solve this, a significant problem arises. The velocities of the expansion and compression pistons, at their respective top dead and bottom dead centers, are equal to zero. This implies that the rates of change of the volume for the expansion and compression spaces are also equal to 0. Revisiting the definitions of the expansion and compression polytropic indices, it is obvious where the problem arises.

$$n_e = -\frac{V_e dP}{p dV_e} \qquad\qquad n_c = -\frac{V_c dP}{p dV_c}$$

Since the derivatives of the volumes are used in the denominator, when their values are zero, the polytropic indices go to infinity. This same problem is observed in the simulations run from Ruijie Li et al. [36], using the same polytropic model from Babaelahi [28]. The comparison between the results can be seen in the following figures:

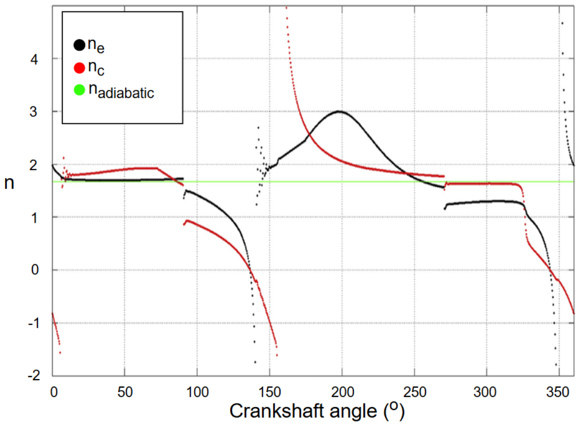

(a) Polytropic indices over crankshaft extracted from [36]

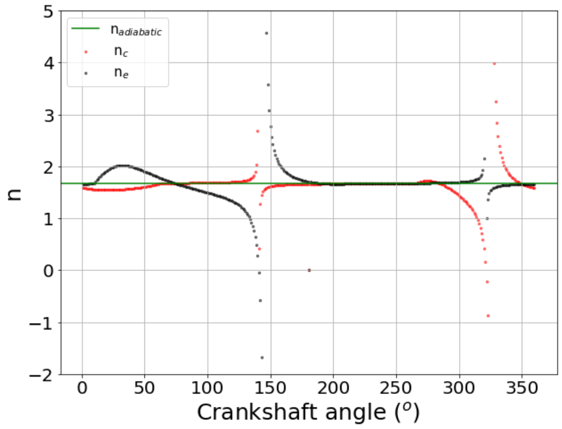

(b) Polytropic indices obtained from simulations

Both figures (Figure 3.6a and Figure 3.6b) depict very similar results from the polytropic model simulations (notice there is a 180-degree shift from one to the other). Aside from the shift, they exhibit identical performance, with the main difference being that the results from the literature have larger peaks, indicating a greater deviation from the adiabatic case.

After several attempts to troubleshoot the model, the problem persisted. The simulation was then run, assuming that the polytropic expansion and compression coefficients are equal to the specific heat capacity ratio (γ) of Helium. This assumption eliminates the polytropic losses of the model. This assumption can be considered close to reality for this specific engine due to several reasons.

First and foremost, the engine model simulated by Babaelahi and Li is the well-known GPU-3 Stirling engine. A fundamental difference between this engine and Electron247's engine is the integration of cylinder-integrated heaters and coolers. This specific characteristic of the GPU-3 directly contradicts the assumptions of adiabatic expansion and compression. As explained in the particular configuration of Electron247, this is not the case for this application, featuring distinct expansion, compression, heater, and cooler spaces.

An analysis is performed after solving the set of equations. The losses of the cylinder walls to the cooling flow of the heat removal circuit are calculated based on the temperature profiles developed in the engine under adiabatic conditions. These profiles are expected to have lower values when the polytropic nature of the compression and expansion spaces is implemented. Since the temperature difference between the working gas and the cooling flow dominates the heat loss, the increased temperatures in the adiabatic case overpredict the total losses during the cycle. Even with this overprediction, the losses peak for an instant around 153 W. When compared to the magnitude of the heat input and output in the engine, this is minimal. More specifically, this loss accounts for less than 0.42% of the heat that is exchanged in the heater, and 0.85% of the heat that is transferred to the cooler. The detailed analysis is presented in Appendix D. Overall, these results prove that the adiabatic assumption of the specified processes is very close to the actual processes taking place in the engine compartments.

Therefore, while the polytropic model is theoretically more advanced, its numerical instability at the piston dead centers combined with the minimal heat loss from the physical cylinders makes the adiabatic assumption a more robust and practical choice for this specific engine geometry, with negligible loss of real-world accuracy.

4

Baseline performance analysis - Model validation

The model is then validated based on experimental measurements from operational Electron247 units. As mentioned earlier, although the original device was designed to operate on a cycle using hydrogen as the working gas, the experiments were conducted with helium due to safety concerns regarding hydrogen leakage.

Baseline configuration

The baseline configuration of the engine is presented in the following table.

This table contains confidential data and has been redacted.

Table 4.1: Baseline configuration and operating parameters of the Electron247 Stirling engine. The table details the geometric dimensions of the heater, cooler, and regenerator, as well as the key operational conditions used for the initial model simulation and validation.

The general dimensions of the configuration are reported from the design specifications of the engine. The inlet temperatures of the heating and cooling streams are approximations based on CFD simulations of the engine from EnergyIntel. The same goes for the mass flows of both streams. The company's design specifications also determine the dimensions of the heat exchangers. Lastly, the clearance volumes are measured from models of the engine, corresponding to the connecting passages between the engine pistons and the heat exchanger’s array.

4.1. Simulation results

The simulation is then run for the baseline configuration. Several performance metrics are extracted from the simulated thermodynamic cycle. The losses are also thoroughly documented and examined to assess their relative magnitudes and impact on overall performance. First, the PV diagram of the engine, as well as for the expansion and compression spaces separately, are plotted.

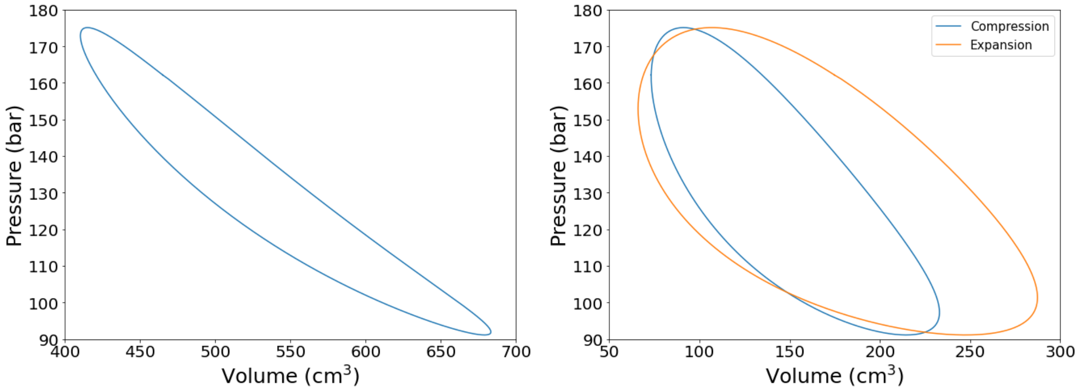

(a) Pressure volume diagram of the engine, operating at the baseline conditions.

(b) Pressure volume diagrams for the compression and the expansion spaces, operating at baseline conditions.

The diagram indicates the engine is operating with pressure oscillating between p_{max}=175.12 bar and p_{min}=91.12 bar. The enclosed area of the PV diagram corresponds to the produced work. As expected, the work produced by the expansion piston is greater than that from the compression piston.

Following the temperatures in different parts of the engine, a plot is generated (Figure 4.2a). The inlet temperatures of sodium and water glycol are observed to be slightly higher and lower than those of the heater and the cooler. The temperatures of the compression and expansion spaces can be observed oscillating between the heater and the cooler temperatures, as expected.

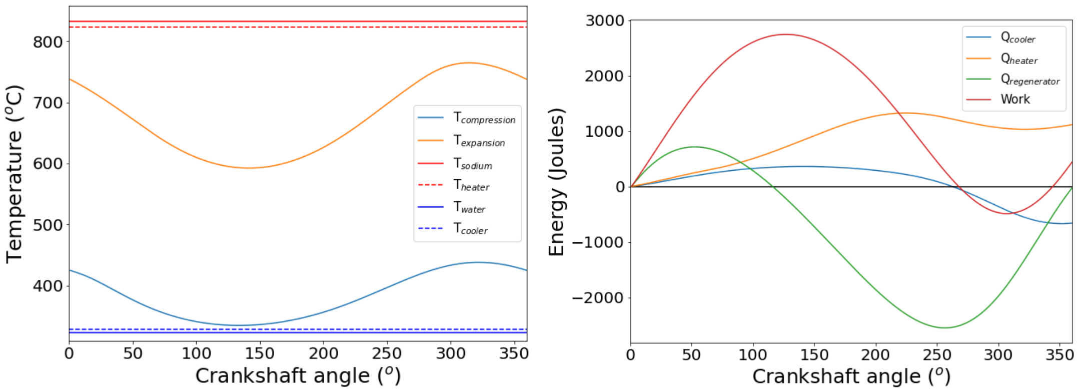

(a) Temperature variations in the compression and expansion spaces, shown relative to the constant temperatures of the heater, cooler, and external heat transfer fluids.

(b) Cumulative energy transfer, illustrating the heat absorbed by the heater, rejected by the cooler, exchanged by the regenerator, and the net work produced.

Figure 4.2: Simulated engine performance over one crankshaft rotation.

The energy-theta diagram is depicted in Figure 4.2b. The plot indicates the accumulated heat transferred and work over the cycle. The final value of the cumulative work curve at a crank angle of 360° represents the net work produced per cycle. An interesting performance metric observed from this figure is the heat transfer to the regenerator matrix. The thermal energy transferred to the matrix throughout the complete cycle is considerably higher than the net work output. As a result, the importance of the regenerator's effectiveness is highlighted by this statistic.

The pressure drop in the individual components is another metric that indicates the most important parameters influencing the engine's performance. Figure 4.3a indicates the increased pressure drop over the regenerator when compared to the heater and the cooler. As in most heat exchangers, increasing the efficiency of heat transfer directly influences the pressure drop in the specific component.

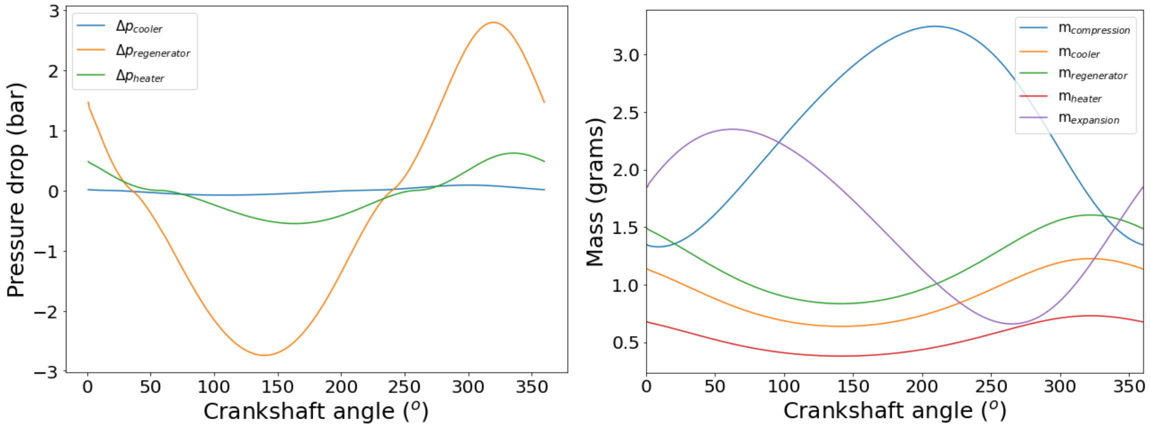

(a) Pressure drop due to fluid friction across the cooler, regenerator, and heater. The regenerator shows the most significant pressure drop.

(b) Variation of working gas mass within each of the five engine compartments (compression, cooler, regenerator, heater, and expansion).

Figure 4.3: Simulated working gas dynamics over one crankshaft rotation.

Figure 4.3b indicates that the mass is varying mostly in the compression and expansion spaces, as expected. Since the volume and temperature in the remaining components are constant over the cycle, the only factor differentiating the mass in these is the pressure in the engine, which is considered constant. As a result, a similar trend in the variation of the mass is observed.

The velocity of the compression and expansion pistons is depicted in Figure 4.4a; these confirm the problem identified in the solution method section of the model, as inconsistencies in polytropic indexes are observed exactly where the top dead and bottom dead centers are encountered (velocity equals zero). The 90-degree phase shift between the expansion and compression pistons is also identified.

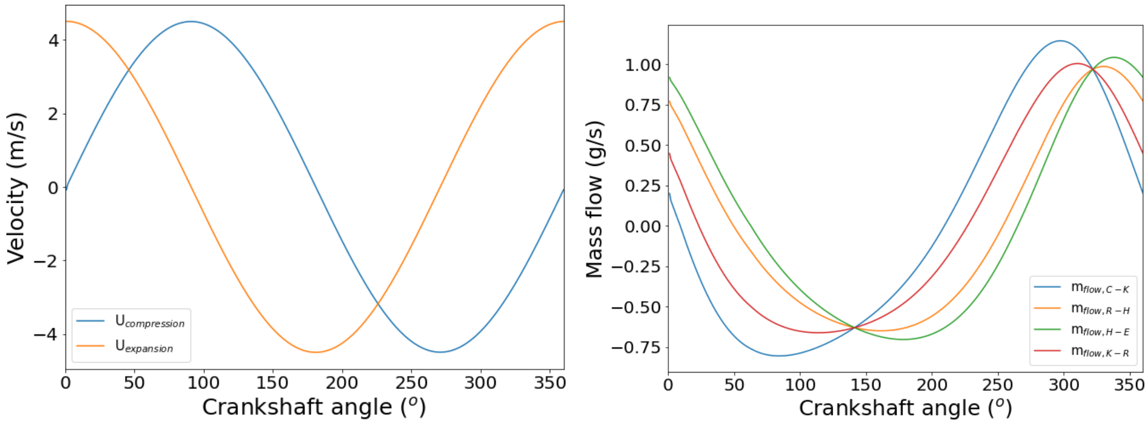

(a) Velocity profiles of the compression and expansion pistons, illustrating their phase difference. Points of zero velocity correspond to the top and bottom dead centers.

(b) Mass flow rates of the working gas at the interfaces between the engine components, showing the oscillating nature of the flow.

Figure 4.4: Piston and working gas flow dynamics.

Finally, the mass flows through the interfaces between engine components are depicted in Figure 4.4b. The importance of this can be seen when comparing it to the pressure loss in components, specifically when the mass flow is high, resulting in an increased pressure drop.

4.2. Performance indices

Following this, the performance indices of the engine are extracted from a set of experimental data at operating conditions of [REDACTED]. The results are presented in the following table.

This table contains confidential data and has been redacted.

Table 4.2: Comparison of model prediction vs. experimental data for the baseline configuration. The table shows the power output, thermal efficiency (η), heat input (Q_h), and sodium outlet temperature for both the simulation and experimental measurements under baseline conditions.

Based on the simulation results, the model overpredicts the performance of the Stirling engine compared to the experimental results. It forecasts a higher power output of [REDACTED] and a thermal efficiency ('e') of [REDACTED] respectively from experiments. These correspond to errors of 5.3% and 8.2% for the power output and efficiency, respectively. The total heat input in the Stirling machine is underestimated by a factor of 2.56%.

The model's predictive accuracy is comparable to that of similar third-order models reported in the literature [27, 28]. The following diagram presents the loss mechanisms modeled and approximated in the model.

Figure contains confidential data and has been redacted.

Figure 4.5: Sankey diagram illustrating the energy balance of the engine for the baseline configuration based on model predictions. It shows the distribution of the total heat input (36.43 kW) into useful work output, heat rejection to the cooler, and various thermal and mechanical losses totaling 7.75 kW.

The model's overprediction is expected and logical, considering several loss parameters that are not modeled in this case.

- Gas leakage through the piston seals. Especially in alpha-type Stirling engines, this affects performance, particularly for extended run times. This is not modeled in the present study due to the unknown pressure distribution in the engine's buffer.
- Engine components' friction is another factor influencing the performance of the engine. However, due to the constant rotational speed of the engine in the performed simulations, the work loss due to friction can be considered a systematic error, which does not influence the consistency of the model.
- While Electron247 is well insulated for reducing any losses to the environment, it is expected that some of the heat is lost to the surroundings, especially from the heater shell.

4.3. Experimental data

The experimental data are extracted from two distinct working units installed in Masdar City, Abu Dhabi, United Arab Emirates. The operational conditions of the engine range from 1400 rpm to 1950 rpm and from 125 bar to 128 bar. These data are used for validating the models.

4.3.1. Data analysis

From the available datasets, only a limited subset contained the necessary parameters for a complete performance evaluation. The reason behind this is the absence of vital data in experimental measurements. More particularly, the heat input of the engine cannot be directly measured; thus, it is obtained based on the inlet and outlet temperatures of the heater using Equation 4.1.

$$Q_{heater} = \dot{m}_{sodium} c_{p,sodium} (T_{in,sodium} - T_{out,sodium}) \tag{4.1}$$

The temperatures are measured during the engine's operation, and the heat capacity of sodium is a material property. However, the sodium mass flow is not available in experimental measurements; as a result, the heat transfer of the heater can not be calculated in post-processing. This quantity is directly needed for calculating the efficiency of the Stirling engine with:

$$\epsilon = \frac{P_{out}}{Q_h} \tag{4.2}$$

Communication with EnergyIntel personnel confirmed that for experimental runs near design conditions (1800 RPM, 125 bar), the sodium mass flow rate was consistent with the design value of [REDACTED]. The model's performance was eventually validated based on these.
Initial data processing was conducted before the model validation; the main reasons behind these operations were the following:

Engine mode filtering

The experimental data sets included data from several modes of operation. The data were filtered to ensure that the engine is evaluated only in the mode of pure discharge.

Invalid data during startup and power down

During the startup and power-down phases of the engine, the system needs several seconds to reach a steady state and for the temperatures to stabilize. As a result, the data corresponding to these timeframes was eliminated.

Data large volume

To decrease simulation times, the data was downsampled from a one-second frequency to a one-minute frequency. Since the engine's primary operational state for this analysis is steady-state discharge, and key parameters like sodium inlet temperature change slowly over time, downsampling from a one-second to a one-minute frequency smooths out high-frequency noise without losing the essential performance trends needed for model validation.

Additionally, several sensor readings that were not needed for validation were also removed from the lists.

Performing these actions provided datasets that included the five necessary quantities for evaluating the engine's performance. Specifically, these quantities included power output, engine rotational speed, engine pressure, and inlet and outlet temperatures of the sodium heat transfer fluid.

4.4. Model Validation

The model validation procedure was then followed for the mathematical model. Three datasets were used, with engine pressure set to 125 bar, and engine rotational speed at 1800 RPM for all datasets.

The model is validated based on its performance (power output and efficiency) with varying sodium inlet temperatures. In reality, the pressure also varies mainly due to the effect of mass leakage. However, the difference from power up to power down is not substantial. Although this is taken into account in the simulations, the effect is not presented here since it is negligible.

Figures contain confidential data and has been redacted.

It can be observed from the graphs that the model can predict the power output and efficiency of the engine accurately. The model is consistent throughout a range of inlet sodium temperatures. The error fluctuates between 0.5% and 9% for the three different datasets. It is evident from the graphs that more factors influence the performance of the engine, which are not documented in the experimental data. Since these are varying but are considered constant in the simulation, there is a large fluctuation of the error between the different datasets. Potential quantities that might vary are the following:

- External ambient temperature, this influences the cooling capabilities of the cooling circuit; thus, a different inlet temperature can be observed in the cooler. Such a change imposes a significant difference on the performance of the engine, which is dictated by the temperature difference between the cold and hot reservoirs.
- Mass of gas in the engine. Since the mass of working gas in the engine is not determined by experiments but by the Schmidt analysis, gas leakage effects potentially impose an error in prediction. If the engine is tested serially without refilling the gas after each test, this introduces an inaccuracy.

This highlights the engine's sensitivity to the working gas mass and cooling side temperature. Future experimental campaigns should prioritize recording these parameters to allow for more precise model validation across different operating conditions. However, the trends of the predictions seem to follow the performance of the actual engine with a justified error margin.

4.4.1. Performance indexes

Following this, several performance indices were calculated to evaluate the predictions' performance based on quantifiable metrics.

MAE (Mean absolute error)

This metric calculates the average of the absolute differences between the predicted and actual values. It gives you an idea of the average magnitude of the errors in your predictions, in the original units of the target variable.

$$\text{MAE} = \frac{1}{n}\sum_{i=1}^{n} |y_{i,experimental} - y_{i,prediction}| \tag{4.3}$$

MSE (Mean squared error)

MSE measures the average of the squares of the errors. By squaring the errors, it penalizes larger errors more heavily than smaller ones.

$$\text{MSE} = \frac{1}{n}\sum_{i=1}^{n} (y_{i,experimental} - y_{i,prediction})^2 \tag{4.4}$$

RMSE (Root mean squared error)

This is the square root of the MSE. The main advantage of RMSE is that its scale is the same as the original target variable. It represents the standard deviation of the prediction errors.

$$\text{RMSE} = \sqrt{\frac{1}{n}\sum_{i=1}^{n} (y_{i,experimental} - y_{i,prediction})^2} \tag{4.5}$$

The performance indices as calculated from the experimental and prediction data can be observed in the following table.

Data	**Pressure**	**MAE**$_{\epsilon}$	**MSE**$_{\epsilon}$	**RMSE**$_{\epsilon}$	**MAE**$_{P_{out}}$	**MSE**$_{P_{out}}$	**RMSE**$_{P_{out}}$
Dataset 1	125 bar	1.70	2.91	1.71	0.65	0.42	0.65
Dataset 2	125 bar	1.58	2.53	1.59	0.43	0.19	0.19
Dataset 3	125 bar	0.51	0.29	0.54	0.23	0.05	0.05

Table 4.3: Prediction error metrics for the thermodynamic model. The table lists the Mean Absolute Error (MAE), Mean Squared Error (MSE), and Root Mean Squared Error (RMSE) for both efficiency (η) and power output (P$_{out}$), calculated by comparing model predictions against three different experimental datasets at 125 bar.

The same conclusion is also evident here, as shown in the data plots. The models accurately predict the engine's performance, with the efficiency of the prediction model compromised or improved by different operational conditions that are not tracked in every distinct case. The Mean Absolute Error (MAE) for power output across the various datasets fluctuates between [redacted]. This means that, on average, the model's power prediction was within 0.65 kW of the measured experimental value, which, for a device operating around 10 kW, represents an acceptable average error of 6.5% at most. The reduced mean squared error for all three datasets indicates consistent model performance across different operating conditions.

The model exhibits similar precision, with an MAE ranging from 0.51% to 1.70% and an RMSE ranging from 0.54% to 1.71%. Notably, the MAE and RMSE values for efficiency are very similar across all three datasets. This proximity indicates that the prediction errors are uniformly distributed and that there are no significant outliers. A model that consistently errs without occasional large deviations is more reliable and predictable.

Based on these performance metrics, the model is deemed sufficiently accurate and robust for use in the subsequent design optimization phase.

5

Design optimization

After completing and validating the model, the optimization procedure takes place. The validated model is then used as the objective function within an optimization algorithm, which executes the model iteratively to converge on a set of optimal solutions. The algorithm of choice is the widely renowned Non-dominated Sorting Genetic Algorithm 2 (NSGA-II). This algorithm was selected due to its well-documented effectiveness and efficiency in solving complex, multi-objective engineering problems. The Python Multi-Objective Optimization (pymoo) package is used to perform the optimization simulations.

5.1. Optimization methodology

The optimization algorithm inputs 10 parameters into the model, the model returns the two optimization objectives, the power output, and the efficiency of the engine.

$$P_{out}, \quad \epsilon = f(d_k, l_k, p_k, d_h, l_h, p_h, d_{omat}, porosity, d_{wire}) \tag{5.1}$$

Where heater length l_h, heater inner tube diameter d_h, heater tube pitch p_h, cooler length l_k, cooler inner tube diameter d_k, cooler tube pitch p_k, regenerator length l_r, regenerator matrix outer diameter d_{omat}, regenerator porosity $porosity$, regenerator wire diameter d_{wire}.

Boundaries

The algorithm randomly selects values for the input parameters between predetermined upper and lower limits for each design variable. Table 5.1 shows the limits used for each parameter.

This table contains confidential data and has been redacted.

Table 5.1: Upper and lower boundaries for design variables in the optimization algorithm. The table specifies the search space for each of the ten geometric parameters, along with the corresponding values of the initial baseline configuration.

For every limit, there is a reason behind the selected boundaries.

- For the lower limit of the inner diameter of the heater and cooler tubes, the value selected is determined by the commercial availability of tubes with a certain tube thickness. Due to the engine operating at relatively high pressure, the walls of the tube must be thick enough to support the pressure loads. Since this factor is not within the scope of the research, the thickness of the tubes is considered constant for both the heater and the cooler. It was determined that the minimum diameter of tubes with adequate tube thickness is [REDACTED] .
- The upper limit for tube thickness is selected to be [REDACTED] . In general, the smaller the diameter, the higher the engine's efficiency, due to both enhanced heat transfer and reduced dead volume in the heat exchangers. The flow friction effects are not substantial enough to have a huge negative effect on the reduced diameter. This is also confirmed by both previous simulations and the optimization procedure results.
- The upper and lower lengths of the heater and cooler are selected as [REDACTED], respectively. These are selected based on the baseline configuration values. Also, a length constraint of the heat exchanger array limits these values.
- The pitch upper and lower limits are also selected based on the baseline configuration. Generally, it is expected that the closer the tubes are packed, the higher the engine's performance. As a result, the upper limits are set but do not have any significant importance. The lower limits are slightly smaller than the baseline configuration and are also constrained.
- The outer diameter limits of the matrix are selected so that they are equidistant from the baseline configuration. The upper limit is set equal to the outer diameter of the tube arrays in the heater and the cooler.
- Both the porosity and the wire diameter of the regenerator are limited within the range that the flow friction and heat transfer correlations are valid.

Constrains

The optimization algorithm also has three constraining conditions, two of them follow the same logic for the heater and the cooler, while the last is a size limitation specifically for the Electron247 device

Heater and cooler pitch

The first and second constraints are in place regarding the geometry generation of the heater and the cooler. More specifically, it is essential that there is sufficient volume for the heat transfer fluids (sodium and water-glycol) to flow through the heat exchangers. This limits the pressure drop and leakage issues of the HTFs. Especially for the sodium due to its reactive nature, this is of great importance. The two constraints are set so that the minimum distance between the outer surfaces of two tubes is not smaller than [redacted] for the heater and cooler, respectively, which are the exact values existing in the baseline configuration.

$$p_h - d_h - 2t_h \geq \text{[redacted] mm} \tag{5.2}$$

$$p_k - d_k - 2t_k \geq \text{[redacted] mm} \tag{5.3}$$

The second limitation applies a space constraint for the total length of the cooler-regenerator-heater array. The maximum length was limited to the length of the baseline configuration ($l_{total} = l_h + l_k + l_r =$ [redacted] mm).

$$l_h + l_r + l_k \leq \text{[redacted] mm} \tag{5.4}$$

Optimization process

Metaheuristic algorithms work by constantly generating, modifying, and evaluating possible solutions by following behaviors typically inspired by nature (nature-inspired metaheuristic algorithms (NIMA)). Metaheuristic algorithms present an ideal approach for optimizing Stirling engines, as they effectively explore complex, non-linear search spaces. The effectiveness of the algorithms relies heavily on two conflicting objectives [37]:

- Exploration-Diversification: This objective is responsible for adequately searching the entire solution space. It is the factor that enables the algorithm to discover diverse, promising solution regions, and it prevents the algorithm from being stuck in a suboptimal area (local optimum).
- Exploitation-Intensification: This procedure enables focusing the search within already identified promising regions.

In multi-objective optimization (such as designing a Stirling engine), some goals conflict with each other. For this specific case, an example is that with the increase of net work output, the losses in the machine also increase, reducing efficiency. Due to these conflicts, there is no single solution that is optimal for all objectives simultaneously.

The concept of evaluating the performance of different solutions hinges on 'Pareto dominance'. A criterion is typically developed to rank the different potential solutions; for example, solution x is considered dominant when compared to solution y based on the hypothesis.

The Pareto-optimal frontier, or Pareto front, is defined as the set of all solutions in the search space that are non-dominated. This means that for every solution on this Pareto front, there is no other feasible solution that can increase the performance on both metrics of the optimization. Consequently, for every solution on this front, there is a trade-off between two performance objectives.

The goal of multi-objective optimization (MOO) is to identify the set of non-dominated solutions that construct the Pareto front.

NSGA-II

NSGA-II, developed by Kalyanmoy Deb et al., is a widely used metaheuristic optimization algorithm that employs an elitist strategy and mechanisms to maintain population diversity. It uses an elitist approach combined with mechanisms for sorting solutions based on non-domination and preserving diversity using a crowding measure [38]. The algorithm follows a systematic generational process to arrive at the Pareto front. The main functionality of the algorithm is affected by six parameters, namely population size N, number of offsprings $n_{\text{offsprings}}$, number of generations n_{gen}, crossover probability $\text{p}_{\text{crossover}}$, mutation probability $\text{p}_{\text{mutation}}$, crossover distribution index $\eta_{\text{crossover}}$. Each one of these parameters influences the convergence time and efficiency of the algorithm.

- The population size N determines the initial number of individual cases examined by the optimization algorithm.
- The number of offsprings $n_{\text{offsprings}}$ determines the number of new cases that are examined in every new generation.
- The number of generations n_{gen} controls the maximum number of new generations that the algorithm will examine. A higher number of generations increases the probability for convergence to the true Pareto front, but it also extends the simulation time.
- Crossover probability $\text{p}_{\text{crossover}}$ is the chance that two selected individual cases from the previous iteration will undergo crossover to introduce a new offspring. The higher the probability, the higher the exploration for new combinations of solutions. A lower probability means that the parents (individuals from previous iterations) will be passed to the next generation of solutions without modification.
- Crossover distribution index $\eta_{\text{crossover}}$ characterizes the similarities of the offspring to their parents. The higher the number, the more similar the offspring is to its parents.
- The mutation probability $\text{p}_{\text{mutation}}$ is the probability that a single characteristic of a generated offspring is randomly altered compared to its parents' characteristics.

5.1.1. Convergence index

The simplest way to ensure convergence to the Pareto front is to increase the number of individual cases examined, N_{cases}.

$$N_{\text{cases}} = N + n_{\text{offsprings}}(n_{\text{gen}} - 1) \tag{5.5}$$

However, the optimization process is a time and computationally extensive process, since the mathematical model needs to be executed for N_{cases}. For reference, a single execution of the model requires approximately six seconds. A complete optimization run of 6,000 evaluations would therefore require approximately 10 hours of computation time.

When the real Pareto front is known, the performance of the optimization algorithm can be evaluated based on how close the generated set of solutions is to the real Pareto front. However, in cases that the Pareto front can only be calculated numerically, the process of evaluating the results becomes more complex. In that case, the results can be evaluated based on the area enclosed by the Hypervolume. The hypervolume is the enclosed area between the generated set of solutions and a reference point.

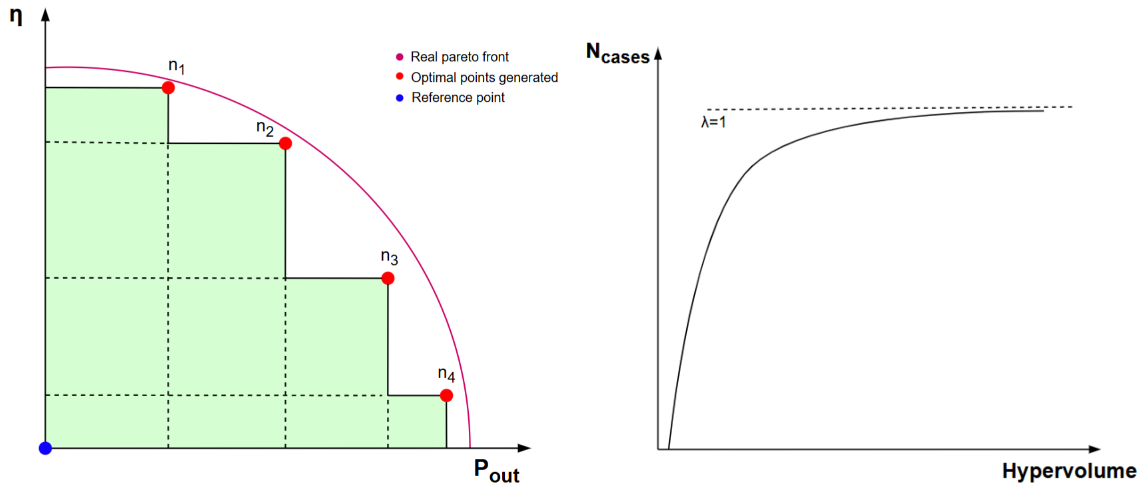

(a) The method with which the hypervolume of a generated set of optima is calculated

(b) The expected evolution of the hypervolume quantity during an optimization procedure.

While the generated set of solutions converges to the real Pareto front, the volume enclosed increases. However, it always remains smaller than or equal to the area enclosed by the real Pareto front. Since the actual Pareto front is unknown, the trends of the hypervolume are monitored. When the increase remains constant with increasing number of cases generated (slope, $\lambda \approx$1), it means that the set of solutions has converged very close to the optimal set of solutions.

5.2. Optimization results

The optimization algorithm is then executed several times to identify the best-performing solution for true convergence. It was identified that the generated Pareto front converges to the real Pareto front with the following parameters:

- Population size N=100
- Number of offsprings $n_{\text{offsprings}}$=35
- Number of generations n_{gen}=200
- Crossover probability $p_{\text{crossover}}$=0.9
- Crossover distribution index $\eta_{\text{crossover}}$=15
- Mutation probability p_{mutation}=20

This translates to a total number of cases of $N_{\text{cases}} = 100 + 35 \times (200 - 1) = 7065$

After execution, the following Pareto front is generated:

Figure contains confidential data and has been redacted.

Figure 5.2: Pareto front generated from the continuous multi-objective optimization. Each point represents an optimal engine design, illustrating the trade-off between maximizing power output and maximizing thermal efficiency.

It is evident from the plot that both the thermal efficiency and the power output of the engine can be considerably increased. The best-performing design in terms of engine thermal efficiency achieves an efficiency of [REDACTED] , while simultaneously indicating a reduced power output of [REDACTED] , compared to the baseline configuration. The convergence to the real Pareto front is evaluated using the hypervolume method; the hypervolume evolution of the simulation is shown in Appendix E.

At the far end of the Pareto front, the best-performing design in terms of power output achieves an increased performance of [REDACTED], while its efficiency remains enhanced to [REDACTED] .

It can be observed that while the power output of the baseline configuration is approximately at the midpoint of the x-axis [REDACTED], all the solutions on the Pareto front indicate an increased efficiency compared to the baseline configuration [REDACTED]. More specifically, out of 100 solutions on the Pareto front, 67 perform better in terms of power output, and all 100 solutions are better in terms of efficiency.

A parallel coordinates plot (PCP) was used to analyze and optimize the geometric parameters of a Stirling engine in relation to its thermal performance.

Figure contains confidential data and has been redacted.

Figure 5.3: Parallel coordinates plot from the continuous optimization results. Each line represents an optimized engine design, displaying the values of the ten input geometric parameters along with their corresponding power output and efficiency. Lines are colored by thermal efficiency, revealing correlations between specific parameter values and engine performance.

The analysis reveals clear trends that inform optimization strategies. Parameters such as the matrix outer diameter (d_{omat}), regenerator length (l_r), heater pitch (p_h), and heater tube diameter (d_h) show a strong positive correlation with thermal efficiency. Specifically, higher efficiencies, approaching EDACTE , are consistently observed when d_{omat} is near [REDACTED] , l_r is around REDACTED , and p_h and d_h approach higher values [REDACTED]. Additionally, longer cooler lengths [REDACTED] also contribute positively to efficiency.

In contrast, other parameters exhibit either a negative or neutral impact on efficiency. For instance, the wire diameter ($d_{w}ire$) tends to be smaller ($\approx$ REDACTED) in high-efficiency cases, likely due to the increased heat transfer surface area associated with finer wires. Similarly, porosity appears to have an optimal range; values around [REDACTED] are associated with the highest efficiency, while both higher and lower porosity values may compromise performance.

Following the initial analysis, the optimization algorithm was adapted to ensure manufacturing feasibility for the engine components. Taking, for example, the cooler's tube internal dimension, the value ranges from [REDACTED]. In a real-world application, these minimal differences do not correspond to realistic manufacturing accuracies of components in such a device. As a result, the optimization algorithm was refined to constrain geometric parameters to discrete, realistic values that align with manufacturing capabilities.

5.2.1. Discrete optimization procedure

The following table represents the accuracy of each dimensional variable

Parameter	d_k **[mm]**	l_k **[mm]**	p_k **[mm]**	d_h **[mm]**	l_h **[mm]**	p_h **[mm]**	d_{omat} **[mm]**	l_r **[mm]**	**porosity [-]**	d_{wire} **[μm]**
Accuracy	0.1	1.0	0.1	1.0	1	1.0	1	1	0.01	1

Table 5.2: Discretization values for geometric parameters in the refined optimization. This table defines the manufacturing accuracy (step size) applied to each design variable, ensuring that the final optimized solutions are physically manufacturable.

The discrete optimization procedure outputs the following Pareto front. The convergence to the real Pareto front is evaluated using the hypervolume method; the hypervolume evolution of the simulation is shown in Appendix E.

Figure contains confidential data and has been redacted.

Figure 5.4: Pareto front generated from the discrete multi-objective optimization. This front represents optimal designs where geometric parameters are constrained to realistic, manufacturable values.

With the same optimization parameters, it can be observed that the algorithm converges closer to the real Pareto front. This is due to the fact that the discrete nature of this problem has fewer possible combinations of solutions. Python, by default, has 28 decimal places of precision. As a result, the initial continuous optimization algorithm can test an almost infinite number of solutions; this is not the case with the discrete algorithm. This can be observed in the slightly enhanced performance of the most efficient and highest power output designs. Namely, the most efficient engine configuration achieves an efficiency of [REDACTED] and a power output of [REDACTED], while the highest power output is [REDACTED], corresponding to an efficiency of [REDACTED] .

The effect of these changes can be observed on the parallel coordinates plot.

Figure contains confidential data and has been redacted.

Figure 5.5: Parallel coordinates plot for the discrete optimization results. It visualizes the relationships between the discrete geometric parameters and the engine's performance, with line colors corresponding to the resulting thermal efficiency.

The influence of each variable does not differ from the parallel coordinate plot of the continuous optimization process; however, a clearer representation can be obtained from the discrete algorithm. For example, the diameter and the pitch of the cooler tubes (d_k and p_k) are equal to the minimum respective minimum boundaries for all cases. This can be attributed to the fact that, due to decreased temperature in the cooler, the frictional losses are minimal; thus, the design of maximum heat transfer capabilities is preferred in all cases.

5.2.2. Cooler dimensions

As depicted in Figure 5.5 and mentioned above, the cooler tube diameter and pitch converge to a single optimal value; however, this is not the case for the cooler length. The most efficient designs show a slightly decreased cooler length. This is attributed to the increased length of the regenerator. Since the regenerator is lengthened, the lengths of the heater and cooler are both reduced to satisfy the maximum summed length constraint of the components. This can be depicted in Figure 5.6

Figure contains confidential data and has been redacted.

Figure 5.6: Influence of cooler and regenerator lengths on engine performance. The plot shows that higher efficiency designs (top-left) are associated with longer regenerators (l_r, indicated by larger point size) and consequently shorter coolers (l_k indicated by color) to satisfy the total length constraint.

5.2.3. Heater dimensions

For the heater dimensions, it is observed that the pitch is either [REDACTED]. It is observed that the most efficient designs feature a larger pitch in combination with an increased tube diameter. This is also combined with an increased length of the cooler.

Figure 5.7 indicates the direct relationship between the heater tubes' outer diameter and pitch. This correlation between the variables is attributed to the discrete nature of the problem, underscoring the need for a discretized algorithm.

Figure contains confidential data and has been redacted.

Figure 5.7: Correlation between heater tube dimensions and engine performance. The plot shows that the most efficient designs (top-left) consistently feature a larger heater tube pitch (p_h, color) combined with a larger heater tube diameter (d_h, point size).

The length of the heater does not exhibit any trends that directly influence the performance metrics of the Stirling engine, as evidenced by the color distribution of the distinct solutions plotted in (Figure 5.8).

Figure contains confidential data and has been redacted.

Figure 5.8: Influence of heater length (l$_h$) on engine performance. The color of the points, representing heater length, is distributed randomly across the Pareto front, indicating that heater length is not directly connected with either power output or efficiency within the tested range.

5.2.4. Regenerator dimensions

The analysis of the results of the regenerator is where the strongest connections between the sizing and performance of the engine are observed. Another analysis of the Pareto front can be observed in the following figure.

Figure contains confidential data and has been redacted.

Figure 5.9: Influence of regenerator outer diameter (d$_{o}mat$) and length (l$_r$) on engine performance. The plot clearly shows that higher efficiency is achieved with a larger regenerator diameter (color) and a greater length (point size). Conversely, higher power output is linked to smaller regenerator volumes.

In detail, Figure 5.9, indicates that with increasing regenerator diameter and increasing length (resulting in total increased regenerator volume), the efficiency of the Stirling engine is greatly improved. At the same time, the decrease in total volume results in a drop in efficiency; however, the engine's power output is improved. This can be attributed once again to the length constraint. With a decreased regenerator length, the lengths of the heater and the cooler can be increased, thereby enhancing the heat performance of the parts. Higher heat input results in increased power output, but decreased engine efficiency due to a drop in the regenerator's heat transfer capabilities.

These conclusions are then combined with the wire diameter and porosity of the regenerator.

Figure contains confidential data and has been redacted.

Figure 5.10: Influence of regenerator wire diameter (d_{wire}) and porosity on engine performance. The plot shows that higher power output designs (bottom-right) are associated with larger wire diameters (point size). In contrast, porosity (color) shows a less distinct trend, with optimal values distributed across the performance range.

More efficient designs indicate a decreased wire diameter, increasing the heat transfer capabilities of the matrix. The values for the porosity of the regenerator are distributed across the domain, with both high-efficiency-low-power output and low-efficiency-high-power output designs featuring low and high porosity matrices.

The absence of a simple linear correlation for all variables, such as for porosity and heater length, highlights the highly non-linear nature of the optimization problem. This complexity justifies the choice of a metaheuristic algorithm like NSGA-II, which does not rely on gradient information and is well-suited for such search spaces.

5.3. Analysis and Selection of Optimized Designs

At this stage, a set of 100 optimized designs has been obtained from the multi-objective optimization process. To proceed with decision-making, three representative solutions are selected based on different performance criteria:

Maximum Efficiency: Since thermal efficiency is a critical metric in evaluating energy storage systems, the first design selected corresponds to the solution with the highest engine efficiency, regardless of its power output.

Efficiency-Constrained Baseline Match: The second design represents the most efficient solution among those producing at least the power output of the baseline system [REDACTED]. This ensures performance parity while maximizing efficiency.

Closest-to-Ideal Solution: The third design is identified as the feasible point closest to the *ideal point* in the normalized objective space. The ideal point is a theoretical construct defined by the maximum power output and maximum efficiency achieved across all solutions, regardless of feasibility. Because power (in kW) and efficiency (dimensionless) operate on different scales, the objective values are normalized using min-max scaling:

$$\hat{f}_1^{(i)} = \frac{f_1^{(i)} - \min_j f_1^{(j)}}{\max_j f_1^{(j)} - \min_j f_1^{(j)}} \quad (5.6) \qquad \hat{f}_2^{(i)} = \frac{f_2^{(i)} - \min_j f_2^{(j)}}{\max_j f_2^{(j)} - \min_j f_2^{(j)}} \quad (5.7)$$

where f_1 and f_2 denote power and efficiency, respectively. The normalized ideal point is thus $(1, 1)$. For each feasible solution, the Euclidean distance to this ideal is computed as:

$$D_i = \sqrt{\left(\hat{f}_1^{(i)} - 1\right)^2 + \left(\hat{f}_2^{(i)} - 1\right)^2}. \tag{5.8}$$

The selected design is the one with the smallest D_i, ensuring a well-balanced compromise between the two objectives.

This structured selection approach enables a balanced comparison of alternatives under different performance preferences, supporting well-informed design decisions. The selected solutions on the Pareto front are shown in Figure 5.11.

Figure contains confidential data and has been redacted.

Figure 5.11: Selection of representative optimal designs from the discrete Pareto front. The plot highlights the ”Maximum Efficiency” design, the ”Closest to Ideal” balanced design, and an ”Efficient” design that matches the baseline power output. The theoretical, non-feasible ”Ideal” point is also shown for reference.

The performance as well as the dimensional parameters of the optimized designs can be observed in Table 5.3.

This table contains confidential data and has been redacted.

Table 5.3: Comparison of optimized designs against the baseline configuration. The table presents the performance metrics and the final geometric parameters for the ”Maximum efficiency,” ”Power constrained,” and ”Closest to ideal” designs, allowing for a direct comparison with the original baseline design.

The results present three distinct cases of improved Stirling engines by dimensional optimizations of the three heat exchangers. Each one of the three cases, presents

5.3.1. Physical importance of the results

The optimization of the Stirling engine’s components has a significant real-world impact, primarily by enhancing the overall round-trip efficiency of the Electron247 thermal energy storage system. This improvement translates directly into substantial environmental benefits, specifically in the reduction of carbon dioxide (CO_2) emissions over the device’s lifespan. By generating more electrical energy from the same amount of stored solar thermal energy, the optimized engine designs reduce the reliance on conventional, fossil-fuel-based grid electricity.

To quantify this benefit, we can calculate the total CO_2 emissions spared by the baseline and optimized designs over the system’s lifetime. This analysis assumes the electrical energy is supplied by solar panels, making the charging process carbon-free [user assumption]. The CO_2 savings come from displacing electricity that would otherwise be drawn from the grid.

- The Electron247 unit stores a maximum of 550 kWh of thermal energy ($kW_{thermal}$).
- The system is rated for over 43,000 full charge-discharge cycles.
- For this analysis, we will use the average greenhouse gas (GHG) emission intensity for electricity generation in Cyprus. According to the European Environment Agency, in 2023, this value was approximated at 575 gCO_2e/kWh [39]. The total lifetime CO_2 spared is then calculated as:

$$\text{CO}_2\text{ Spared (tons)} = \text{Electrical Output per Cycle} \times 43\,000 \text{ cycles} \times 0.575\,\frac{\mathrm{tons}}{\mathrm{MWh}} \tag{5.9}$$

The analysis reveals that even the baseline configuration of a single Electron247 unit is projected to spare over 3900 tons of CO_2 during its operational life compared to using grid electricity, excluding the CO_2 emissions associated with manufacturing the device.

However, the optimization yields dramatic improvements. The ”Maximum Efficiency” design, with its enhanced [REDACTED] efficiency, spares an additional 1093 tons of CO_2 compared to the baseline, a 28% increase in environmental benefit. Similarly, the ”Power Constrained” and

This table contains confidential data and has been redacted.

Table 5.4: CO_2 emissions analysis for baseline and optimized designs.

”Closest to Ideal” designs, which offer a balance between efficiency and power output, result in an additional 854 and 801 tons of avoided CO_2 emissions, respectively.

These results underscore the physical importance of the optimization process. A seemingly modest increase in percentage points of efficiency, when scaled over the long operational lifetime and high cycle count of the energy storage device, translates into a significant and tangible reduction in greenhouse gas emissions. This highlights the crucial role of targeted engineering enhancements at the component level in maximizing the environmental and economic returns of renewable energy storage technologies.

6

Conclusions and recommendations

6.1. Conclusions

This research successfully developed and validated a robust thermodynamic model for the alpha-type Stirling engine used in the Electron247 thermal energy storage system. The development and validation of the third-order thermodynamic model provided a reliable and computationally efficient tool for exploring a complex, multi-dimensional design space. The key conclusions drawn from this work are as follows:

1. A robust, third-order quasi-steady thermodynamic model was successfully developed and validated for the alpha-type Stirling engine. The model proved to be a computationally efficient and reliable tool, with a predictive error of less than 7% against experimental data, enabling the detailed exploration of a complex, multi-dimensional design space without the immediate need for extensive CFD or physical prototyping.
2. The optimization has conclusively shown that the baseline engine design is suboptimal. The results reveal a clear Pareto-optimal frontier of designs that substantially outperform the current configuration. The maximum achievable thermal efficiency was increased from a baseline of [redacted] to [redacted] —a relative increase of over 27%. This confirms that component geometry is a primary limiting factor in the current system and that significant gains in round-trip efficiency are attainable.
3. The optimization process provided deep insight into the complex interplay between component geometries. The regenerator's dimensions (total volume, porosity, and wire diameter) were unequivocally identified as the most influential parameters. A clear trade-off emerged:
    - High Efficiency is driven by a large regenerator volume (maximized diameter and length) with fine wire mesh. This configuration maximizes the heat transfer area and thermal mass, thereby improving the regenerator's effectiveness and reducing the heat that the heater must supply.
    - High Power Output is favored by a smaller regenerator volume. This reduces flow losses (pressure drop) and, due to the system's overall length constraint, allows for larger heater and cooler components, which increases the total heat input and rejection capacity of the engine, thereby increasing the work per cycle.
4. Three different improved designs are selected, taking into account the selling points and most important properties of an energy storage device.

5. The direct consequence of improving the engine's thermal efficiency is a significant reduction in the environmental footprint of the energy storage system. By generating more electricity from the same amount of stored thermal energy, the optimized designs spare an additional 800 to 1,100 tons of CO2 emissions per unit over a 30-year operational lifetime. This enhancement strengthens the technology's position as a viable and impactful solution for decarbonizing the energy sector.

6.2. Recommendations

1. To further close the gap between simulation and real-world performance, the thermodynamic model should be enhanced to incorporate second-order loss mechanisms. Future work should focus on integrating:
    - Gas Leakage models for pressure-driven leakage through the dynamic seals of the expansion and compression pistons. For this, it is essential to obtain extensive information on the pressure distribution in the connecting buffer between the expansion and compression spaces of the engine.
    - Account for conductive heat loss through the engine's structural components and convective/radiative losses from the external casing to the ambient environment.
2. To support the development of more sophisticated models, future experimental validation campaigns should be more comprehensive. It is crucial to implement sensors and data logging for:
    - Dynamic Working Gas Mass: Continuously track the mean cycle pressure and average temperatures in all five engine volumes to more accurately estimate the mass of the working fluid in real-time.
    - Ambient Temperature: Log the ambient temperature, as this directly defines the external heat loss conditions and is fundamental to engine performance.
3. The optimization framework can be extended to explore an even wider solution space. Future studies should consider:
    - Operational Parameters: Include engine speed (RPM) and mean charge pressure as variables in the optimization to find the optimal working parameters between geometry and operating conditions.
    - Working Fluid Analysis: Re-evaluate the use of hydrogen as the working fluid, coupling the thermodynamic model with advanced sealing technologies to determine if its superior thermal properties can be leveraged to enhance performance further.
4. It is strongly recommended to proceed with the manufacturing and empirical testing of a prototype based on the "Closest to Ideal" solution [REDACTED]. This design represents the most strategic choice as it delivers a substantial improvement in both power and efficiency, making it a commercially robust and well-rounded product enhancement. This physical prototype will serve as the final and most crucial validation of the model's predictions.
5. Given the regenerator's demonstrated sensitivity and pivotal role in engine performance, manufacturing precision is paramount. It is recommended to establish rigorous quality control protocols for the regenerator matrix, focusing on:
    - Sourcing wire mesh with a highly consistent wire diameter and weave to ensure the target porosity is achieved uniformly throughout the matrix.

    - Developing a precise assembly process to prevent bypass flow channels and ensure uniform packing density, which is critical for realizing the predicted heat transfer effectiveness and flow characteristics.

6. Before committing to a final design for mass production, a comprehensive techno-economic analysis should be conducted. This analysis should weigh the performance gains of the top candidate designs against any potential increases in manufacturing cost or complexity associated with the new specifications (e.g., larger regenerator, finer tube dimensions). This will ensure the selected design optimizes not just for thermodynamic performance but also for commercial viability and return on investment.

Bibliography

[1] United Nations. The paris agreement, 2015.

[2] IRENA. World energy transitions outlook 2024: 1.5°c pathway, 2024.

[3] Shell International Limited. The energy security scenarios, 2023.

[4] IEA. Share of renewable electricity generation by technology, 2000-2030, 2024. Licence: CC BY 4.0.

[5] Kedar Balasubramanian. Germany's duck curve – integrating renewables into smart grids, 2023.

[6] Michael Sterner and Michael Specht. Power-to-gas and power-to-x—the history and results of developing a new storage concept. *Energies*, 14(20), 2021.

[7] IRENA. World energy transitions outlook 2023: 1.5°c pathway, volume 1, 2023.

[8] Guruprasad Alva, Lingkun Liu, Xiang Huang, and Guiyin Fang. Thermal energy storage materials and systems for solar energy applications. *Renewable and Sustainable Energy Reviews*, 68:693–706, 2017.

[9] Ioan Sarbu and Calin Sebarchievici. A comprehensive review of thermal energy storage. *Sustainability*, 10(1), 2018.

[10] Huili Zhang, Jan Baeyens, Gustavo Cáceres, Jan Degrève, and Yongqin Lv. Thermal energy storage: Recent developments and practical aspects. *Progress in Energy and Combustion Science*, 53:1–40, 2016.

[11] Ioan Sarbu and Calin Sebarchievici. A comprehensive review of thermal energy storage. *Sustainability*, 10(1), 2018.

[12] Sameer Khare, Mark Dell'Amico, Chris Knight, and Scott McGarry. Selection of materials for high temperature latent heat energy storage. *Solar Energy Materials and Solar Cells*, 107:20–27, 2012.

[13] Annette Heinzel, Wolfgang Hering, Jürgen Konys, Luca Marocco, Karsten Litfin, Georg Müller, Julio Pacio, Carsten Schroer, Robert Stieglitz, Leonid Stoppel, Alfons Weisenburger, and Thomas Wetzel. Liquid metals as efficient high-temperature heat-transport fluids. *Energy Technology*, 5(7):1026–1036, 2017.

[14] G Walker. *Stirling engines*. Oxford University Press,New York, NY, 01 1980.

[15] W R Martini. Stirling engine design manual. Technical report, Washington Univ., Richland (USA). Joint Center for Graduate Study, 04 1978.

[16] Bancha Kongtragool and Somchai Wongwises. A review of solar-powered stirling engines and low temperature differential stirling engines. *Renewable and Sustainable Energy Reviews*, 7(2):131–154, 2003.

[17] I Urieli and D M Berchowitz. Stirling cycle engine analysis, Jan 1984.

[18] Mojtaba Babaelahi and Hoseyn Sayyaadi. Simple-ii: A new numerical thermal model for predicting thermal performance of stirling engines. *Energy*, 69:873–890, 2014.

[19] Andreas Fritsch, Cathy Frantz, and Ralf Uhlig. Techno-economic analysis of solar thermal power plants using liquid sodium as heat transfer fluid. *Solar Energy*, 177:155–162, 2019.

[20] Abudusaimi Yakufu, Zhou Yang, Yuting Xu, and Qiang Wang. Research on thermal-hydraulic characteristics of liquid sodium versus molten salt as a fluid in heat exchanger. In *2023 7th International Conference on Power and Energy Engineering (ICPEE)*, pages 434–438, 2023.

[21] Madjid Sarvghad, Teng C. Ong, Stuart Bell, Raihan Rumman, Salar Delkasar Maher, Jack W. Woodcock, Geoffrey Will, Gunther Andersson, David A. Lewis, and Theodore A. Steinberg. On the compatibility of liquid sodium as heat transfer fluid for advanced concentrated solar thermal energy systems. *Solar Energy Materials and Solar Cells*, 246:111897, 2022.

[22] Konstantin Mikityuk. Heat transfer to liquid metal: Review of data and correlations for tube bundles. *Nuclear Engineering and Design*, 239(4):680–687, 2009.

[23] Rui Zhang, Wang Zhenying, Zhenhong Wang, Tingting Ren, and Jiangwu Shi. Theoretical investigation on the fully developed turbulent heat transfer characteristics of liquid sodium. *Frontiers in Energy Research*, 8, 02 2020.

[24] Kenneth M. Armijo and Charles E. Andraka. Phenomenological studies on sodium for csp applications: A safety review. *AIP Conference Proceedings*, 1734(1):040001, 05 2016.

[25] Madjid Sarvghad, Teng Cheong Ong, Stuart Bell, Raihan Rumman, Salar delkasar, Jack Woodcock, Geoffrey Will, Gunther Andersson, David Lewis, and Theodore Steinberg. On the compatibility of liquid sodium as heat transfer fluid for advanced concentrated solar thermal energy systems. *Solar Energy Materials and Solar Cells*, 246:111897, 07 2022.

[26] W M Kays and A L London. *Compact heat exchangers*. McGraw-Hill,New York, NY, 01 1984.

[27] Mojtaba Babaelahi and Hoseyn Sayyaadi. A new thermal model based on polytropic numerical simulation of stirling engines. *Applied Energy*, 141:143–159, 2015.

[28] Mojtaba Babaelahi and Hoseyn Sayyaadi. Modified psvl: A second order model for thermal simulation of stirling engines based on convective–polytropic heat transfer of working spaces. *Applied Thermal Engineering*, 85:340–355, 2015.

[29] W.A. Khan, J.R. Culham, and M.M. Yovanovich. Convection heat transfer from tube banks in crossflow: Analytical approach. *International Journal of Heat and Mass Transfer*, 49(25):4831–4838, 2006.

[30] V. Gnielinski. New equations for heat and mass transfer in the turbulent flow in pipes and channels. *NASA STI/Recon Technical Report A*, 41(1):8–16, January 1975.

[31] F. de Monte, G. Galli, and F. Marcotullio. An analytical oscillating-flow thermal analysis of the heat exchangers and regenerator in stirling machines. In *IECEC 96. Proceedings of the 31st Intersociety Energy Conversion Engineering Conference*, volume 2, pages 1421–1427 vol.2, 1996.

[32] S.C. Costa, Harritz Barrutia, Jon Ander Esnaola, and Mustafa Tutar. Numerical study of the heat transfer in wound woven wire matrix of a stirling regenerator. *Energy Conversion and Management*, 79:255–264, 2014.

[33] P D Roach and K J Bell. Analysis of pressure drop and heat transfer data from the reversing flow test facility. Technical report, Argonne National Lab. (ANL), Argonne, IL (United States), 05 1989.

[34] David Gedeon and J. Gary Wood. Oscillating-flow regenerator test rig: Hardware and theory with derived correlations for screens and felts. 1996.

[35] John B Heywood. Combustion engine fundamentals. *1ª Edição. Estados Unidos*, 25:1117–1128, 1988.

[36] Ruijie Li, Lavinia Grosu, and Wei Li. New polytropic model to predict the performance of beta and gamma type stirling engine. *Energy*, 128:62–76, 2017.

[37] Fawad Ahmed, Hulin Huang, Shoaib Ahmed, and Xin Wang. A comprehensive review on modeling and performance optimization of stirling engine. *International Journal of Energy Research*, 44, 03 2020.

[38] K. Deb, A. Pratap, S. Agarwal, and T. Meyarivan. A fast and elitist multiobjective genetic algorithm: Nsga-ii. *IEEE Transactions on Evolutionary Computation*, 6(2):182–197, 2002.

[39] European Environment Agancy. Greenhouse gas emission intensity of electricity generation in europe, 2025.

[40] S. W. Churchill and M. Bernstein. A correlating equation for forced convection from gases and liquids to a circular cylinder in crossflow. *Journal of Heat Transfer*, 99(2):300–306, 05 1977.

A

Technical specifications of Electron247

A.1. Performance and electrical specification

Feature	Value
Nominal Power – Output	13.0 kW$_e$ | 30kW$_{th}$
Continuous Operating Power – Output	12.1 kW$_e$
Rated Energy Capacity	165kWh$_e$ | 550kWh$_{th}$
Voltage - Input/Output	400 Vac - 3 phase+N+PE
Voltage Tolerance - Input/Output	+/- 10%
Frequency	50 Hz / 60 Hz
AC Current at nominal power - Output	20 A
Maximum AC Current - Output	42.5 A
Maximum AC Current - Input	145 A
Maximum Charging Power	100 kW
Charging duration (at Maximum Charging Power)	6h - 0h+1h

Table A.1: Performance and Electrical Specifications

Feature	Value
Communication	Modbus TCP/IP
Remote Monitoring Support	Yes
Local Data Recording	Data logger

Table A.2: Communication Specifications

A.2. Communication specification

A.3. Environmental specification

Feature	Value
Operating Ambient Temperature	-10°C to +50°C, 14°F to 122°F
Storage Ambient Temperature	-30°C to +70°C, -22°F to 158°F
Relative Humidity	100%
Operating Altitude	<2000m (6562 ft) above sea level
Maximum Snow Load	1kN/m^2
Noise	<70dB

Table A.3: Environmental Specifications

A.4. Mechanical specification

Feature	Value
Dimensions E247-V1 (LxWxH m)	L3.65xW2.67xH2.81
Total weight	8025kg
Cooling principle (engines)	Dry cooling

Table A.4: Mechanical Specifications

A.5. Lifetime and durability

Feature	Value
Number of full Cycles	>43000
Depth of discharge	100%
Lifespan	30 years

Table A.5: Lifetime and durability

B

Geometry generation algorithm

The functionality as well as the algebraic equations used for the derivation of the geometry of the heat exchangers is explained in this chapter.

B.1. Array of tubes generation

Initially, the function creates a grid of possible tube locations (x,y) within the boundary, based on the pitch p and the shell dimensions H and W. For the triangular layout, the horizontal distance between tubes is equal to the pitch; in contrast, the vertical distance of distinct tube rows is not equal to p, but:

$$\text{Vertical distance} = \frac{\sqrt{3}}{2}p \tag{B.1}$$

To maintain the triangular arrangement, the generation of each row of tubes is also shifted by half of the pitch $\frac{p}{2}$. After generating potential tube positions based on these, it is checked whether the tube fits within the shell boundaries. Initially, within the length and height of the shell, with:

$$x_{min} = -\frac{W}{2} + \frac{D_{tube,out}}{2} \tag{B.2}$$

$$x_{max} = \frac{W}{2} - \frac{D_{tube,out}}{2} \tag{B.3}$$

$$y_{min} = -\frac{H}{2} + \frac{D_{tube,out}}{2} \tag{B.4}$$

$$y_{max} = \frac{H}{2} - \frac{D_{tube,out}}{2} \tag{B.5}$$

Finally, the following condition is checked; if this is fulfilled, it means that the tubes also fit within the rounded corners of the rectangle, with r being the shell corner radius:

$$\left(|x| < \frac{W}{2} - r - \frac{D_{out}}{2}\right) \vee \left(|y| < \frac{H}{2} - r - \frac{D_{out}}{2}\right) \vee \left(\sqrt{\left(|x| - \left(\frac{W}{2} - r\right)\right)^2 + \left(|y| - \left(\frac{H}{2} - r\right)\right)^2} + \frac{D_{out}}{2} \leq r\right) \tag{B.6}$$

The tube location (x,y) is then added to the array of tubes. Following, the number of tubes can be calculated. Having the number of tubes along with their positions means that essential quantities of the heat exchanger, mainly the heat transfer area, can be calculated; this step is necessary for modeling the heat exchangers.

B.2. Shell side flow modeling

The velocities of the heat transfer fluids at the shell side of the heat exchangers can be obtained by analyzing the array of tubes generated previously. For this, the total free area along the YZ plane (not obstructed by tubes) distance in the shell needs to be calculated:

$$A_{free} = L(y_{total} - y_{obstructed}) \tag{B.7}$$

Assuming the flow of the heat transfer fluids is uniform over the length of the heat exchangers, the area is obtained by multiplying the total free vertical distance by the length of the heat exchanger. Initially, the total height in the shell is calculated with:

$$y_{total}(x) = 2\left[\left(\frac{H}{2} - r\right) + \sqrt{r^2 - \left(|x| - \left(\frac{W}{2} - r\right)\right)^2}\right] \tag{B.8}$$

Then, the obstructed vertical distance from tubes, is determined. First a condition is checked on wether there are tubes at the specific x coordinate with:

$$|x - x_{tube}| \leq \frac{d_{out}}{2} \tag{B.9}$$

Following, if a tube is present, the obstructed by tubes height is calculated with:

$$h_{obstructed} = \sum_{-\frac{W}{2}}^{\frac{W}{2}} \sqrt{\left(\frac{d_{out}}{2}\right)^2 - (x - x_{tubes})^2} \tag{B.10}$$

With mass conservation, the total velocity of the heat transfer fluids can be obtained with:

$$V = \frac{\dot{m}_{fluid}}{\rho_{fluid} A_{free}} \tag{B.11}$$

C

Model derivation

The process followed to obtain the set of ordinary differenctial equations is thourouhgly explained below:

Polytropic indices

Due to the polytropic nature of the model, the state of the compression and the expansion spaces can be modeled obeying the following relation:

$$pV^n = constant \tag{C.1}$$

The polytropic indices for the compression and expansion spaces can be obtained by differentiating Equation C.1 and solving for n:

$$p(nV^{n-1}dV) + V^n dp = 0$$

$$n_e = -\frac{V_e dP}{pdV_e} \quad n_c = -\frac{V_c dP}{pdV_c} \tag{C.2}$$

Equation of state

Moving on to defining the system of differential equations, it is assumed that the working gas follows ideal gas behavior. This assumption is based on the fact that the engine always operates away from the critical point of the working gas. For reference, the critical point of hydrogen is at 33.2 K and 12.0 bar, while that of helium is 5.2 K and 2.26 bar. As a result, the ideal gas law can be used as the equation of state:

$$pV = mRT \tag{C.3}$$

Differentiating Equation C.3 results in:

$$\frac{dp}{d\theta}\frac{1}{p} + \frac{dV}{d\theta}\frac{1}{V} = \frac{dm}{d\theta}\frac{1}{m} + \frac{dT}{d\theta}\frac{1}{T} \tag{C.4}$$

Neglecting the gas leakage effects through the piston seals, the mass of the working gas is assumed to be constant and equal to:

$$m_c + m_k + m_r + m_h + m_e = M \tag{C.5}$$

Substituting the equation of state (Equation C.3) in the mass conservation equation Equation C.5 results in:

$$p = \frac{MR}{\frac{V_c}{T_c} + \frac{V_k}{T_k} + \frac{V_r}{T_r} + \frac{V_h}{T_h} + \frac{V_e}{T_e}} \tag{C.6}$$

Moving on, differentiating the mass conservation results in:

$$\frac{dm_c}{d\theta} + \frac{dm_k}{d\theta} + \frac{dm_r}{d\theta} + \frac{dm_h}{d\theta} + \frac{dm_e}{d\theta} = 0 \tag{C.7}$$

For the heater, cooler, and regenerator, the temperature and the volume are considered constant throughout the complete cycle; thus, their respective derivatives are equal to zero, which reduces the derivative of the equation of state Equation C.4 to:

$$\frac{dm_{k,r,h}}{d\theta} = \frac{dp}{d\theta}\frac{m_{k,r,h}}{p} = \frac{dp}{d\theta}\frac{V_{k,r,h}}{RT_{k,r,h}} \tag{C.8}$$

Substituting in the derivative of the mass conservation Equation C.7:

$$\frac{dm_c}{d\theta} + \frac{dm_e}{d\theta} + \frac{dp}{d\theta}\frac{1}{R}\left(\frac{V_k}{T_k} + \frac{V_r}{T_r} + \frac{V_h}{T_h}\right) = 0 \tag{C.9}$$

The volumes and temperatures of the three heat exchangers are constant and known. The goal is to obtain the equations for m_c and m_e to determine an explicit equation for the pressure differential. These can be done by specifying the energy equation for the compression and expansion spaces.

Energy equation

The generalized system of equations is derived by applying the principle of energy conservation to the five control volumes. The generalized control volume is depicted in Figure C.1a:

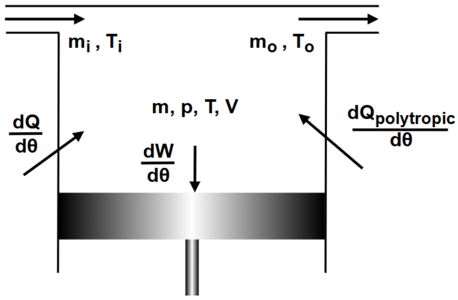

(a) A generalized control volume showing heat, work, and mass-energy transfer terms.

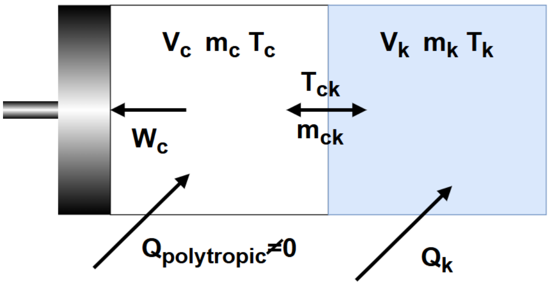

(b) Specific application to the interface between the compression space (c) and the cooler (k).

The derived energy conservation equation equals:

$$\frac{dQ}{d\theta} - \frac{dQ_{polytropic}}{d\theta} + c_p T_i m_i - c_p T_o m_o = \frac{dW}{d\theta} + c_v \frac{d(mT)}{d\theta} \tag{C.10}$$

Where:

- c_v and c_p are the constant volume and constant pressure-specific heat capacities, respectively.
- $T_{i,o}$, and $m_{i,o}$ are the input and output temperature of the flows in the cell, and the corresponding mass.

- It is assumed that the difference in velocity and altitude between input and output flows are negligible; thus, the kinetic and potential energy terms usually included in the energy equation are neglected.

The double-indexed variables T_{ck} and m_{ck} correspond to the temperatures at and the mass flows through the interfaces between control volumes. These are defined on every interface and simulate the oscillating nature of the working gas in the engine. The temperatures of these interfaces depend on the direction of the flow, being equal to the temperature of the adjacent control volume. The following equations are used to define these:

$$\mathrm{T_{ck}} = \begin{cases} T_c, & \dot{m}_{\mathrm{ck}} > 0 \\ T_k, & \dot{m}_{\mathrm{ck}} < 0 \end{cases} \qquad \mathrm{T_{he}} = \begin{cases} T_h, & \dot{m}_{\mathrm{he}} > 0 \\ T_e, & \dot{m}_{\mathrm{he}} < 0 \end{cases}$$

The heat addition and work terms are defined differently for each control volume. Compared to Urieli's model, an additional term is added ($\frac{Q_{polytropic}}{d\theta}$). This term corresponds to the losses induced in the differential equations. The calculation of the polytropic loss factor in the energy equation requires taking into account both the thermodynamic nature of the processes and the heat transfer characteristics inside and outside of the expansion and compression cylinders. The heat transfer from the internal flow to the external cooling flow can be approximated by:

$$\dot{Q}_{cooling} = \frac{T - T_{cooling}}{R_t} \tag{C.11}$$

Where:

- $T_{cooling}$ is the average temperature of the cooling flow
- $R_t = \frac{1}{A_i h_i} + \frac{ln(d_o/d_i)}{2\pi k_w L} + \frac{1}{A_o h_o}$ is the total thermal resistance between the cooling flow and the working gas. In this equation, the A_i, A_o, and h_i, h_o are the inner and outer heat transfer areas and convective heat transfer coefficients, k_w is the thermal conductivity of the wall, d_o and d_i are the outer and inner diameters of the cylinder. L is the height of the cylinder.

The polytropic process heat loss is defined as:

$$Q_{polytropic} = mC_n \left(\frac{R_{conv,i}}{R_t} \right) (T - T_{cooling}) \tag{C.12}$$

Where:

- $C_n = c_v \frac{n-k}{n-1}$ is the polytropic specific heat
- $R_{conv,i} = \frac{1}{A_i h_i}$ is the thermal resistance between the working gas and the cylinder.

Substituting these equations in the general energy conservation equation and simplifying results in:

$$\cancelto{0}{\frac{dQ}{d\theta}} - C_n \left(\frac{R_{conv,i}}{R_t} \right) (T - T_{cooling}) \frac{dm_c}{d\theta} - mC_n \left(\frac{R_{conv,i}}{R_t} \right) \frac{dT_c}{d\theta} + c_p T_{ck} \frac{dm_c}{d\theta} = p \frac{dV_c}{d\theta} + c_v \frac{d(m_c T_c)}{d\theta}$$

$$C_n \left(\frac{R_{conv,i}}{R_t} \right) (T_{cooling} - T) \frac{dm_c}{d\theta} - mC_n \left(\frac{R_{conv,i}}{R_t} \right) \frac{dT_c}{d\theta} + c_p T_{ck} \frac{dm_c}{d\theta} = p \left(1 + \frac{c_v}{R} \right) \frac{dV_c}{d\theta} + \frac{c_v V_c}{R} \frac{dp}{d\theta}$$

$$\left(\frac{C_n R_{conv,i}}{c_p T_{ck} R_t} \right) (T_{cooling} - T) \frac{dm_c}{d\theta} - \left(\frac{mC_n R_{conv,i}}{c_p T_{ck} R_t} \right) \frac{dT_c}{d\theta} + \frac{dm_c}{d\theta} = \frac{p}{RT_{ck}} \frac{dV_c}{d\theta} + \frac{V_c}{R\gamma T_{ck}} \frac{dp}{d\theta}$$

$$\frac{dm_c}{d\theta} = \frac{\frac{p}{RT_{ck}}\frac{dV_c}{d\theta} + \frac{V_c}{R\gamma T_{ck}}\frac{dp}{d\theta} + \left(\frac{m_c C_{nc} R_{conv,i}}{c_p T_{ck} R_t}\right)\frac{dT_c}{d\theta}}{1 + \left(\frac{C_{nc} R_{conv,i}}{c_p T_{ck} R_t}\right)\left(T_{cooling} - T_c\right)} \tag{C.13}$$

In a similar manner, the mass differential for the expansion space can be obtained:

$$\frac{dm_e}{d\theta} = \frac{\frac{p}{RT_{he}}\frac{dV_e}{d\theta} + \frac{V_e}{R\gamma T_{he}}\frac{dp}{d\theta} + \left(\frac{m_e C_{ne} R_{conv,i}}{c_p T_{he} R_t}\right)\frac{dT_e}{d\theta}}{1 + \left(\frac{C_{ne} R_{conv,i}}{c_p T_{he} R_t}\right)\left(T_{cooling} - T_e\right)} \tag{C.14}$$

The boundary conditions are derived from the mass balance, $dm_c = m_{ck}$ and $m_{rh} = m_{he} - dm_h$

Substituting these in the expression of differential pressure, the following is obtained:

$$\frac{dp}{d\theta} = -\frac{\dfrac{\frac{p}{T_{ck}}\frac{dV_c}{d\theta} + R\left(\frac{m_c C_{nc} R_{conv,i}}{c_p T_{ck} R_t}\right)\frac{dT_c}{d\theta}}{1 + \left(\frac{C_{nc} R_{conv,i}}{c_p T_{ck} R_t}\right)\left(T_{cooling} - T_c\right)} + \dfrac{\frac{p}{T_{he}}\frac{dV_e}{d\theta} + R\left(\frac{m_e C_{ne} R_{conv,i}}{c_p T_{he} R_t}\right)\frac{dT_e}{d\theta}}{1 + \left(\frac{C_{ne} R_{conv,i}}{c_p T_{he} R_t}\right)\left(T_{cooling} - T_e\right)}}{\dfrac{\frac{V_c}{\gamma T_{ck}}}{1 + \left(\frac{C_{nc} R_{conv,i}}{c_p T_{ck} R_t}\right)\left(T_{cooling} - T_c\right)} + \dfrac{\frac{V_e}{\gamma T_{he}}}{1 + \left(\frac{C_{ne} R_{conv,i}}{c_p T_{he} R_t}\right)\left(T_{cooling} - T_e\right)} + \left(\frac{V_k}{T_k} + \frac{V_r}{T_r} + \frac{V_h}{T_h}\right)} \tag{C.15}$$

The temperature differentials for compression and expansion space are obtained by rearranging Equation C.4:

$$\frac{dT_c}{d\theta} = T_c\left(\frac{dp}{d\theta}\frac{1}{p} + \frac{dV_c}{d\theta}\frac{1}{V_c} - \frac{dm_c}{d\theta}\frac{1}{m_c}\right) \tag{C.16}$$

$$\frac{dT_e}{d\theta} = T_e\left(\frac{dp}{d\theta}\frac{1}{p} + \frac{dV_e}{d\theta}\frac{1}{V_e} - \frac{dm_e}{d\theta}\frac{1}{m_e}\right) \tag{C.17}$$

Following **??** is applied to the cooler, regenerator, and heater. The work and temperature differentials are equal to 0:

$$\frac{dQ}{d\theta} + c_p T_i m_i - c_p T_o m_o = \frac{\cancelto{0}{dW}}{\cancel{d\theta}} + c_v T\frac{dm}{d\theta} = \frac{V c_v}{R}\frac{dp}{d\theta} \tag{C.18}$$

$$\frac{dQ_k}{d\theta} = \frac{V_k c_v}{R}\frac{dp}{d\theta} - c_p\left(T_{ck} m_{ck} - T_{kr} m_{kr}\right) \tag{C.19}$$

$$\frac{dQ_r}{d\theta} = \frac{V_r c_v}{R}\frac{dp}{d\theta} - c_p\left(T_{kr} m_{kr} - T_{rh} m_h\right) \tag{C.20}$$

$$\frac{dQ_h}{d\theta} = \frac{V_h c_v}{R}\frac{dp}{d\theta} - c_p\left(T_{rh} m_{rh} - T_{he} m_{he}\right) \tag{C.21}$$

Finally, the total work can be computed along with the distinct compression and expansion piston contributions:

$$\frac{dW_c}{d\theta} = p\frac{dV_c}{d\theta} \tag{C.22}$$

$$\frac{dW_e}{d\theta} = p\frac{dV_e}{d\theta} \tag{C.23}$$

$$\frac{dW}{d\theta} = \frac{dW_c}{d\theta} + \frac{dW_e}{d\theta} \tag{C.24}$$

D

Cylinder losses

Assuming the polytropic indices n$_c$ and n$_e$ equal to gamma implies that the expansion and compression phases of the cycle are considered adiabatic processes. After solving the model, an analysis is performed to test this hypothesis. The analysis estimates the total losses of the gas in the expansion and compression cylinders to the surrounding cooling flow. This can be done with Equation D.1

$$\dot{Q}_{\textbf{cyl}} = \frac{T_{\text{gas}} - T_{\text{cooling}}}{R_{\text{total}}} \tag{D.1}$$

Where:

- T_{gas} is the gas temperature in the cylinders
- T_{cooling} is the average temperature of the cooling flow around the cylinders
- R_{total} is the total thermal resistance between the gas and the cooling flow

The total thermal resistance is approximated with Equation D.2

$$R_{\text{total}} = \frac{1}{h_{\text{gas}} A_{\text{in}}} + \frac{ln(d_{\text{out}}/d_{\text{in}})}{2\pi k_{\text{cyl}} L_k} + \frac{1}{h_{\text{cooling}} A_{\text{out}}} \tag{D.2}$$

Due to the piston movement, the areas change constantly with crank angle; the same holds for the convective heat transfer coefficient of the gas in the cylinder. It can be calculated with Equation D.3 [28].

$$h_{\text{gas}} = \begin{cases} 0.023(\text{Re})^{0.8}(\text{Pr})^{0.4}\frac{k}{D_{\text{h}}} & \text{Re} > 10,000 \\ 0.023(\text{Re})^{0.8}(\text{Pr})^{0.4}\frac{k}{D_{\text{h}}}\left[1 + \left(\frac{D_{\text{h}}}{L}\right)^{0.07}\right] & 2100 < \text{Re} \leq 10,000 \\ 1.86 \times (\text{Gz})^{0.333}\frac{k}{D_{\text{h}}} & \text{Re} \leq 2100 \text{ and Gz} > 10 \\ 5 & \text{Re} \leq 2100 \text{ and Gz} \leq 10 \end{cases} \tag{D.3}$$

With Gz, the Graetz number defined with Equation D.4.

$$Gz = RePr\frac{d_{in}}{L} \tag{D.4}$$

Due to the nature of the convective heat transfer coefficient function, there are abrupt changes in the magnitude of this quantity. After it is calculated, the values are fitted to a polynomial of 15th degree. The results for both the compression and expansion spaces can be observed in Figure D.1

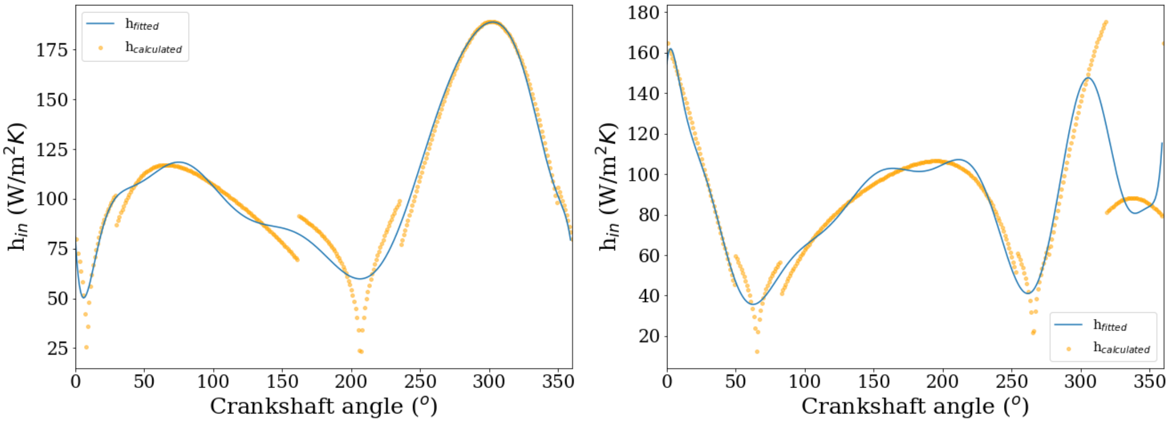

(a) The convective heat transfer coefficient between the compression cylinder inner surface and the working gas in the engine over the crank angle. The fitted curve can be observed in blue while the orange dots represent the data.

(b) The convective heat transfer coefficient between the expansion cylinder inner surface and the working gas in the engine over the crank angle. The fitted curve can be observed in blue while the orange dots represent the data.

Figure D.1: Convective heat transfer coefficients over crank angle.

It can be observed that the coefficient in the expansion space reaches a higher value than the compression space.

The heat transfer coefficient of the cooling flow is determined with the Churchill and Bernstein correlation for flows around cylinders [40].

$$Nu_D = 0.3 + \frac{0.62 Re_D^{1/2} Pr^{1/3}}{\left[1+\left(\frac{0.4}{Pr}\right)^{2/3}\right]^{1/4}}\left[1+\left(\frac{Re_D}{282000}\right)^{5/8}\right]^{4/5} \tag{D.5}$$

The average velocity of the fluid around the cylinder is determined by CFD simulations of the cooling circuit from EnergyIntel (V = 5 m/s). The properties of the water-glycol mixture are also obtained from EnergyIntel documentation. The resulting convective heat transfer coefficients are equal to 4405.2 W/m^{2}K for the compression cylinder and 4595.0 W/m^{2}K for the expansion cylinder. The difference between these is attributed to the difference in outer cylinder diameter of the spaces. Following the heat transfer rate between the cooling flow and the cylinders is calculated and depicted in Figure D.2. Due to the increased temperature difference between the expansion cylinder and the cooling flow, the total energy loss to the cooling circuit is dominated by the hot side of the engine.

Overall, the heat transfer rate between the cylinders and the cooling flow is maximized right after the bottom dead center of the expansion piston (θ=0). This is attributed to the fact that the heat-exchanging surface between the working gas and the cylinder has a high value, while the flow is not stagnant (which is the case at the bottom dead center). The velocity of the flow is directly connected to the magnitude of the heat transfer coefficient. Even though the heat transfer coefficient reaches a higher value around θ=180, the heat exchanging area is greatly reduced at that point, due to the expansion piston being positioned at the top dead center.

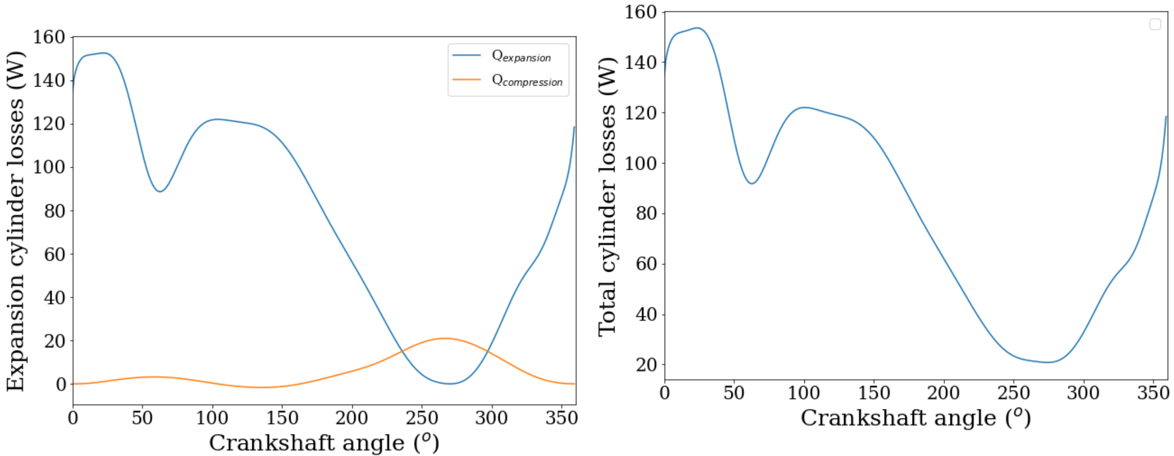

(a) The total heat transfer rate between the working gas and cooling flows for both the compression and expansion pistons.

(b) The total heat transfer rate between the cooling flow and the cylinders, it can be observed that it is dominated by the expansion cylinder losses.

Figure D.2: Heat losses through the cylinder walls.

The magnitude of the total heat transfer reaches a value of 153.6 W. Comparing this to the total heat input of [REDACTED] for the baseline configuration, there is a two orders of magnitude difference between these.

The results of this analysis prove the fact that the assumption for adiabatic expansion and compression phases in the engine, is well justified, and is aligned with the real world performance of the Stirling engine.

E

Convergence criteria of algorithms

The hypervolumes for both the continuous algorithm and discrete optimization procedure can be observed in Figure E.1 and Figure E.2.

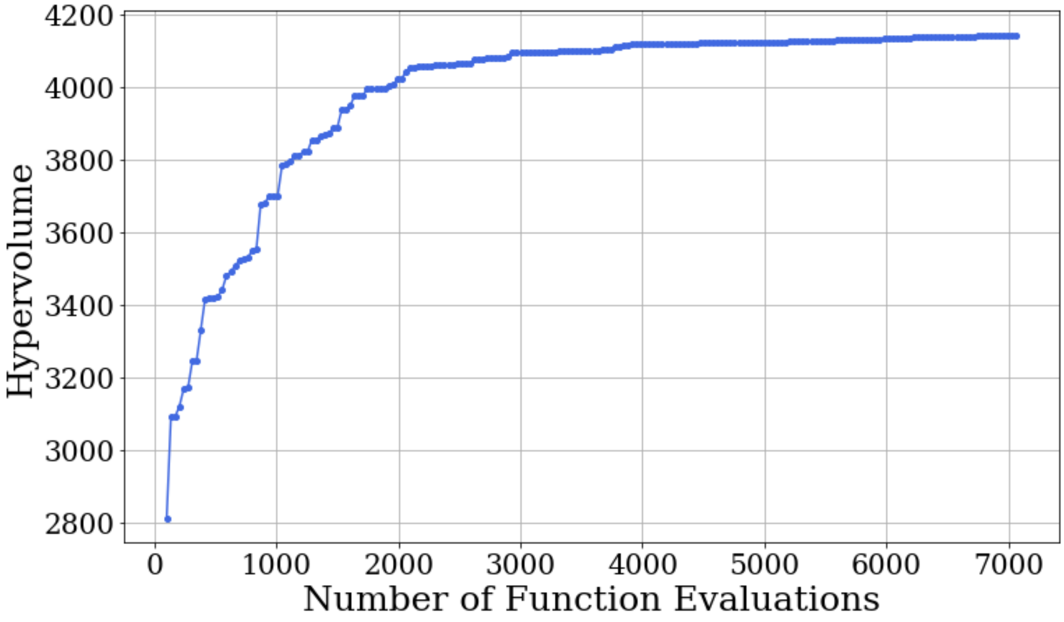

Figure E.1: The hypervolume evolution over the number of valuations of the objective function for the continuous optimization algorithm.

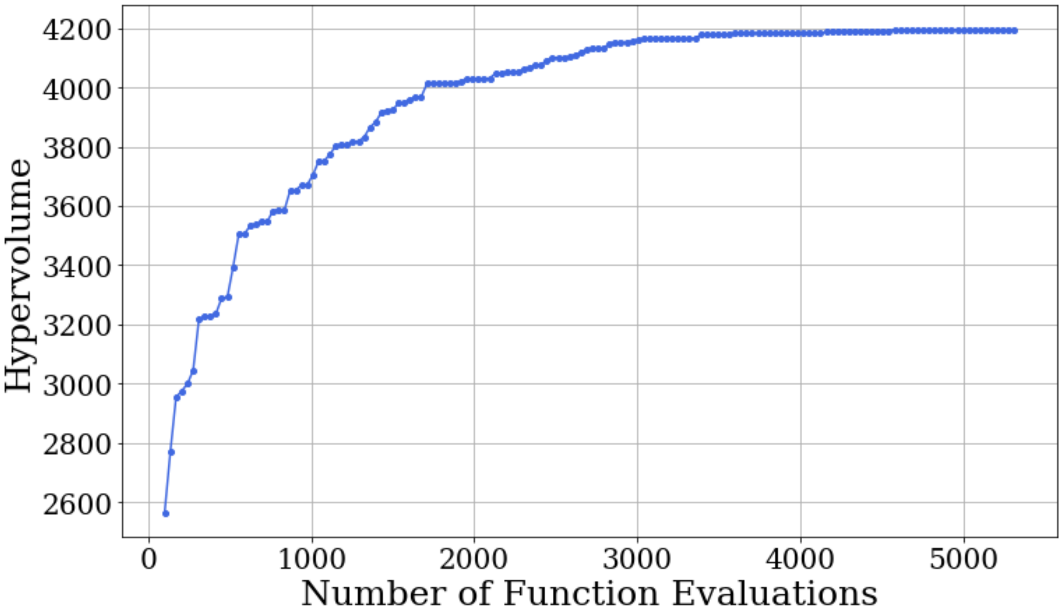

Figure E.2: The hypervolume evolution over the number of valuations of the objective function for the discrete optimization algorithm.

It is evident from both plots that the hypervolume for both algorithms converges to a value for a number of iterations towards the end of the process; the optimization procedures approximate the solutions of the real Pareto front.